The Shape of the Bacterial Ribosome Exit Tunnel Affects Cotranslational Protein Folding

Renuka Kudva[1], Pengfei Tian[4], Fatima Pardo Avila[3], Marta Carroni[1,2], Robert B. Best[4], Harris D. Bernstein[5], Gunnar von Heijne[1,2*]

[1]Department of Biochemistry and Biophysics, Stockholm University, SE-106 91 Stockholm, Sweden

[2]Science for Life Laboratory Stockholm University, Box 1031, SE-171 21 Solna, Sweden

[3] Department of Structural Biology, Stanford University, Stanford, CA 94085, USA

[4]Laboratory of Chemical Physics and [5]Genetics and Biochemistry Branch, National Institute of Diabetes and Digestive and Kidney Diseases, National Institutes of Health, Bethesda, MD 20892, USA

*To whom correspondence should be addressed:

Phone: Int+46-8-16 25 90. E-mail: gunnar@dbb.su.se

Classification: Biological sciences; Biochemistry

Key words: protein folding, ribosome, cotranslational, arrest peptide, uL23, uL24

Running title: Cotranslational protein folding

Abbreviations: AP = arrest peptide, PTC= Peptidyl Transferase Centre

Abstract

The *E.coli* ribosome exit tunnel can accommodate small folded proteins, while larger ones fold outside. It remains unclear, however, to what extent the geometry of the tunnel influences protein folding. Here, using *E. coli* ribosomes with deletions in loops in proteins uL23 and uL24 that protrude into the tunnel, we investigate how tunnel geometry determines where proteins of different sizes fold. We find that a 29-residue zinc-finger domain normally folding close to the uL23 loop folds deeper in the tunnel in uL23 Δloop ribosomes, while two ~100-residue protein normally folding close to the uL24 loop near the tunnel exit port fold at deeper locations in uL24 Δloop ribosomes, in good agreement with results obtained by coarse-grained molecular dynamics simulations. This supports the idea that cotranslational folding commences once a protein domain reaches a location in the exit tunnel where there is sufficient space to house the folded structure.

38 **Introduction**

39 A large fraction of cellular proteins likely start to fold cotranslationally in the
40 ~100 Å long exit tunnel in the ribosomal large subunit (1-3), before they emerge
41 into the cytosolic environment. In *E. coli* ribosomes, portions of the 23S rRNA
42 and a few universally conserved proteins line the exit tunnel, Fig. 1A. The tunnel
43 proteins uL4, uL22, and uL23 consist of globular domains that are buried within
44 the rRNA, and β-hairpin loops that protrude into the tunnel (4). These loops help
45 stabilize the tertiary structure of 23S rRNA (5) and contribute towards the
46 unique geometry of the tunnel (2, 6, 7). uL24 and uL29 are located near the end
47 of the tunnel, and a hairpin loop in uL24 forms a finger-like structure that
48 partially obstructs the tunnel exit port.

49 Inspired by observation that protein domains fold in different parts of the exit
50 tunnel depending on their molecular weight (8-12), we now ask what role the
51 geometry of the exit tunnel plays in determining where these domains fold. To
52 explore this question, we employ the same arrest peptide-based approach (and
53 coarse-grained MD simulations) used in our previous studies of cotranslational
54 protein folding (13, 14), but with ribosomes that carry deletions in either the
55 uL23 or the uL24 hairpin loop. Our findings provide strong evidence that the
56 tunnel geometry determines where in the tunnel a protein starts to fold.

57 **Results and Discussion**

58 *The folding assay*

59 Our experimental set-up, Fig. 1B, exploits the ability of the SecM translational
60 arrest peptide (AP) (15) to act as a force sensor (16-18), making it possible to
61 detect the folding of protein domains in the exit tunnel (13, 18). In brief, the

62 domain to be studied is cloned, via a linker, to the AP, *L* residues away from its C-
63 terminal proline. The AP is followed by a C-terminal tail, to ensure that arrested
64 (*A*) nascent chains can be cleanly separated from full-length (*FL*) chains by SDS-
65 PAGE. Constructs with different *L* are translated in the PURE *in vitro* translation
66 system (19), and the fraction full-length protein (f_{FL}) is determined for each *L*.
67 For linkers that, when stretched, are long enough to allow the protein to reach a
68 part of the exit tunnel where it can fold, force will be exerted on the AP by the
69 folding protein, reducing stalling and increasing f_{FL}. (20), Fig. 1C. A plot of f_{FL} vs. *L*
70 thus shows where in the exit tunnel a protein starts to fold and at which linker
71 length folding no longer causes increased tension in the nascent chain. A number
72 of earlier studies have provided strong support for the notion that the dominant
73 peak in a f_{FL} profile corresponds to folding into the native state (as opposed to,
74 *e.g.*, non-specific compaction of the nascent chain), at least for small, single-
75 domain proteins (11, 13, 14, 20-22).

76 *uL23 Δloop and uL24 Δloop ribosomes*

77 The *E. coli* strains HDB143 (uL23 Δloop; uL23 residues 65-74 deleted) and
78 HDB144 (uL24 Δloop; uL24 residues 43-57 deleted) have previously been shown
79 to be viable (23), as is a strain where uL23 has been replaced by a homologue
80 from spinach chloroplast ribosomes that also lacks the β-hairpin loop (24, 25).
81 These strains were used to purify high-salt-washed ribosomes that were used to
82 translate proteins in the commercially available PURExpress® Δ-Ribosome kit.
83 Analysis of the purified ribosomes by SDS-PAGE and Western blotting
84 demonstrated the expected size differences compared to wildtype for the uL23
85 Δloop and uL24 Δloop proteins, Figure 1- figure supplement 1.

86 *Cryo-EM structure of uL23 Δloop ribosomes*

87 The loop deleted in the uL24 Δloop ribosomes does not interact with
88 neighboring parts of the ribosome, Fig. 2A, and hence its removal would not be
89 expected to alter the structure of other parts of the exit tunnel. In contrast, the
90 loop deleted in uL23 Δloop ribosomes is located deep in the exit tunnel, Fig. 2B,
91 ~ 40-50 Å from the exit and it is not clear *a priori* whether its removal may cause
92 rearrangements in other tunnel components. For this reason, we determined a
93 cryoEM structure of the uL23 Δloop 70S ribosome at an average resolution of 3.3
94 Å, Fig. 2C, Figure 2- figure supplement 1, and found that the shape of the tunnel
95 remains unchanged in the uL23 Δloop ribosome when compared with wildtype
96 (WT) *E. coli* ribosomes, except for an increase in volume resulting from the
97 absence of the uL23 loop Fig. 2C-D. We estimated this increase using the POVME
98 algorithm (26, 27). Compared to WT *E. coli* ribosomes, the tunnel volume
99 increases by 2,064 $Å^3$ in uL23 Δloop ribosomes, see Video 1, about 1/3 of the size
100 of ADR1a (5,880 $Å^3$) calculated by the same method.

101 *ADR1a folds deeper in the exit tunnel in uL23 Δloop but not in uL24 Δloop*
102 *ribosomes*

103 ADR1a constructs of different linker lengths (*L*) were translated in the
104 PURExpress® Δ-Ribosome kit supplemented with purified WT, uL23 Δloop, or
105 uL24 Δloop ribosomes, either in the presence of 50 μM Zn^{2+} (to promote folding
106 of ADR1a) or in the presence of 50 μM of the zinc-specific chelating agent TPEN
107 (to prevent folding of ADR1a; TPEN is required to remove residual amounts of
108 Zn^{2+} from the PURE lysate) (Figure 3A, Figure 3- figure supplements 1-4).
109 Translation rates in PURE are ~10-fold slower than *in vivo* (28), but since the

110 proteins studied here fold on micro-to-millisecond time scales, i.e., considerably
111 faster than the *in vivo* translation rate, it is safe to assume that the folding
112 reaction has time to equilibrate between each translation step both *in vivo* and in
113 the PURE system.

114 Similar to previous results (13), we saw efficient stalling when ADR1a was
115 translated in the presence of TPEN at $L \geq 19$ residues, Figure 3- figure
116 supplement 8. Further, there is a slight but significant increase in f_{FL} at $L = 17$
117 residues in the presence of TPEN (hence not related to folding); this has been
118 observed before (13) and we hypothesize that it is due to a weakening in the
119 arrest potency of SecM by the ADR1a residues that abut the AP in this construct
120 (see Figure 3- figure supplement 9 for sequences). To correct for this effect, we
121 calculated $\Delta f_{FL} = f_{FL}(Zn^{2+}) - f_{FL}(TPEN)$, Fig. 3A. In the presence of Zn^{2+}, the Δf_{FL}
122 profiles for WT and uL24 Δloop ribosomes are very similar: Δf_{FL} starts to
123 increase around L = 20-21 residues and peaks at L = 25 residues (grey and blue
124 curves). In contrast, for the uL23 Δloop ribosomes, Δf_{FL} starts to increase already
125 at L = 17 residues and peaks at L = 21-24 residues (red curve). To quantify these
126 differences, for each f_{FL} curve we calculated the linker lengths characterizing the
127 onset and end of the peak (L_{onset} and L_{end}; defined as the L-values for which the
128 curve has half-maximal height, as indicated in Fig. 3A), as well as the L-value
129 corresponding to the peak of the curve (L_{max}), Table 1.

130 A previous cryo-EM study demonstrated that the 29-residue ADR1a domain folds
131 deep inside the ribosome exit tunnel in a location where it is in contact with the
132 uL23 loop (13), Fig. 2B. The additional space available in uL23 Δloop ribosomes
133 makes it possible for ADR1a to start to fold at 3-4 residues shorter linker lengths

134 (L_{onset}). Assuming an extended conformation of the linker segment (~3Å per
135 residue), ADR1a folds ~9-12 Å deeper in the exit tunnel in uL23 Δloop ribosomes
136 than in WT ribosomes.

137 *Spectrin and titin domains fold deeper in the exit tunnel in uL24 Δloop ribosomes*

138 The 109-residue α-spectrin R16 domain has been shown to fold cotranslationally
139 at $L \approx 35$ residues, in close proximity to uL24 in the exit port region (14). As seen
140 in Fig. 3B and Table 1, with both WT and uL23 Δloop ribosomes, R16 has L_{onset} =
141 31 residues and L_{max} = 35 residues (gray and red curves). For the uL24 Δloop
142 ribosomes however, L_{onset} = 29 residues and L_{max} = 33 residues (Table 1),
143 suggesting that that spectrin R16 folds ~6-7 Å deeper in the exit tunnel when the
144 uL24 loop does not obstruct the tunnel exit port.

145 Similar results were obtained for the 89-residue titin I27 domain, Fig. 3C.
146 Previous studies have shown that the I27 domain folds at linker lengths L = 35-
147 39 residues and that it folds in about the same location as does spectrin R16, in
148 close proximity to the uL24 loop (20). The f_{FL} profile is not affected by the uL23
149 loop deletion, but folding commences at ~4 residues shorter linker lengths in
150 uL24 Δloop ribosomes, similar to R16 (Table 1).

151 *Coarse-grained molecular dynamics simulations*

152 In order to provide a more detailed structural framework for interpreting the f_{FL}
153 profile results, we performed coarse-grained molecular dynamics simulations of
154 the cotranslational folding of ADR1a, spectrin R16, and titin I27 in WT,
155 uL23 Δloop, and uL24 Δloop ribosomes, using a recently described model that
156 allows us to calculate f_{FL} profiles from the simulations (20). The essence of the
157 method is that the simulations are used to determine folded and unfolded

158 populations at each linker length, and the forces associated with them.
159 Combining this information with the experimentally determined force-
160 dependent escape rate of the AP from the ribosome (18) in a kinetic model
161 allows f_{FL} to be calculated. Simulated (full lines) and experimental (dashed lines)
162 f_{FL} profiles are shown in Fig. 3D-F, and detailed simulation results, together with
163 representative snapshots from the simulations of the folded domains at $L \approx L_{onset}$,
164 are shown in Figure 3- figure supplement 10. For all three proteins, the L_{onset}
165 values are well reproduced by the simulations, both in WT and Δloop ribosomes.
166 L_{max} values are also well captured by the simulations for ADR1a (WT ribosomes)
167 and I27 (both WT and uL24 Δloop ribosomes), but are shifted to somewhat
168 lower values in the R16 simulations.

169 The simulated ADR1a f_{FL} profile for uL23 Δloop ribosomes, while showing an
170 early onset of folding in agreement with the experimental profile, has a much
171 smaller L_{max} value. We also performed a simulation using a ribosome model with
172 a smaller deletion in the uL23 loop (residues 70-72; red curve marked by X's); in
173 this case, the peak in the simulated profile extends between L_{onset} and L_{end} values
174 that are more similar to the experimental profile for uL23 Δloop ribosomes. The
175 shape of the f_{FL} profile for ADR1a is clearly highly sensitive to fine structural
176 details of the exit tunnel and therefore somewhat difficult to reproduce by
177 coarse-grained simulations.

178 In summary, both the experimental and simulation results are consistent with
179 the idea that proteins start to fold as soon as they reach a part of the exit tunnel
180 that is large enough to hold the folded protein. Judging from the f_{FL} profiles, the
181 29-residue ADR1a domain folds approximately ~9-12 Å deeper in the exit tunnel

182 in uL23 Δloop ribosomes than in WT and uL24 Δloop ribosomes, while the 89-
183 and 109-residue titin and spectrin domains fold ~6-10 Å deeper inside the
184 tunnel in uL24 Δloop ribosomes than in WT and uL23 Δloop ribosomes; the
185 corresponding values estimated from the simulations are ~6Å for ADR1a and
186 ~13-15 Å for I27 and R16 (Figure 3- figure supplement 10 panel B).

187 Both the uL23 and uL24 loops thus serve to reduce the space available for
188 folding, but in different parts of the exit tunnel. The uL24 loop is particularly
189 interesting in this regard. In bacterial ribosomes, it partially blocks the tunnel
190 exit port, closing off what would otherwise be a wide, funnel-like opening, Fig.
191 2a, and thereby prevents domains of $M_w \geq 10$ kDa from folding inside the exit
192 tunnel. It is conserved (in length, if not in sequence) in bacterial ribosomes,
193 Figure 1- figure supplement 2, suggesting that this will be the case not only for *E.*
194 *coli* ribosomes but for bacterial ribosomes in general. Eukaryotic ribosome
195 tunnels have different geometries owing to expansion segments in their rRNA as
196 well as an increased number of proteins and a wider exit port (29, 30); uL24 is
197 among the most divergent proteins compared to bacteria (31). We therefore
198 expect the precise relation between the onset of folding and protein M_w to be
199 somewhat different in eukaryotic ribosomes, as also suggested by a recent study
200 (32).
201

202 **Acknowledgements**

203 This work was supported by grants from the Knut and Alice Wallenberg
204 Foundation, the Swedish Cancer Foundation, and the Swedish Research Council
205 to GvH, and PT, RBB and HDB were supported by the Intramural Research

206 program of the National Institute of Diabetes and Digestive and Kidney Diseases
207 of the NIH. FPA was supported by NIH grant R35GM122543. The cryo-EM data
208 were collected at the Swedish National Cryo-EM Facility funded by the Knut and
209 Alice Wallenberg Foundation, the Family Erling Persson Foundation and the
210 Science for Life Laboratory. This work utilized the computational resources of
211 the NIH HPC Biowulf cluster (http://hpc.nih.gov).

212 **Materials and Methods**

213 Key Resources

Reagent type (species) or resource	Designation	Source or reference	Identifiers	Additional information
strain, strain background (*Escherichia coli*)	HDB140, HDB143, HDB144, Strain background MC4100	10.1111/j.1365-2958.2010.07325.x	CGSC#: 6152	Strains used to isolate high-salt washed ribosomes in this study.
antibody	uL23, uL24	10.1111/j.1365-2958.2010.07325.x	NA	1:8000 dilution used (incubated for one hour). Secondary antibody: Mouse (1:20,000 dilution incubated for one hour). Nitrocellulose membrane blocked with 5% Milk in TBS-T for an hour.
peptide, recombinant protein	uL23 Δ loop, uL24 Δ loop	10.1111/j.1365-2958.2010.07325.x	UniProtKB-P0ADZ0 (rplW) UniProtKB-P60624 (rplX)	Referred to as HDB 143 and HDB 144 in original paper. Refers to genes rplWΔ65-74 and rplXΔ43-57 respectively.
commercial assay or kit	GeneJET Plasmid miniprep kit	Thermo Fisher Scientific RRID:SCR_008452	Cat no. K0502	Used to purify plasmids
commercial assay or kit	PURExpress ® Δ Ribosome kit	New England Biolabs	Cat no. E3313S	Kit was supplemented with ribosomes purified in the lab.

				Translation carried out at 37°C for 20 min.
software, algorithm	EasyQuant	doi: 10.1038/nsmb.2376	NA	Used to quantify relative fraction full-length of translated protein from SDS-PAGE
software, algorithm	cryoSPARC version v2	Structura Biotechnology Inc	NA	Used for ab-initio reconstruction of uL23Δloop ribosomes. The following operations were carried out as part of the cryoSPARC workflow: 2D classification, Ab initio reconstruction, Homogeneous refinement, Sharpening and map flipping to correct for handedness, local resolution.
software, algorithm	UCSF ChimeraX		SCR_015872	Used to make Figure 2A
software, algorithm	UCSF Chimera v. 1.12	J Comput Chem. 2004 Oct;25(13): 1605-12.	SCR_004097	Used to visualise the cryoEM map, fit PDB models 3JBU, 4YBB to check for differences in maps. Used to make figures.
software, algorithm	Jalview v 2.10.4	doi: 10.1093/bioinformatics/btp033	SCR_006459	Use for generating multiple sequence alignments of uL23 and uL24 in the supplementary figures.
chemical	Potassium acetate	Sigma-Aldrich (SCR_008988)	Cat no. P1190	Source of potassium ions to stabilise ribosomes
chemical	Magnesium acetate	Sigma-Aldrich (SCR_008988)	Cat no. M5661	Source of Magnesium ions to stabilise ribosomes
chemical	cOmplete protease	Sigma-Aldrich	Cat no. 04693116001	Used as a protease inhibitor during cell

	inhibitor cocktail	(SCR_008988)		lysis to obtain ribosomes
chemical	N,N,N′,N′-Tetrakis(2-pyridylmethyl)ethylenediamine	Sigma Aldrich (SCR_008988)	Cat no. P4413	Used to chelate Zn for the -Zn reactions in the ADR1 plot.
chemical	threo-1,4-Dimercapto-2,3-butanediol DL-Dithiothreitol	Sigma Aldrich (SCR_008988)	Cat no. DTT-RO	Reducing agent added to buffers during ribosome purification and as a reductant for SDS-PAGE
chemical	Tris Base	Sigma-Aldrich (SCR_008988)	Cat no. T1503	Buffering agent during ribosome preparation
chemical	35S Methionine	Perkin-Elmer	Cat no. NEG009T001MC	35S Methionine is incorporated into the protein during in vitro translation and aids detection by phosphorimaging.

214

215

216 *Enzymes and Chemicals*

217 The PURExpress® Δ Ribosome kit was purchased from New England Biolabs
218 (Cat no. E3313S). The components used to prepare Lysogeny Broth (LB
219 Medium) for ribosome isolation were obtained from BD Biosciences and all other
220 chemicals used were sourced from Merck Sigma Aldrich. (^{35}S) Methionine was
221 purchased from Perkin Elmer. Bis-Tris gels and plasmid isolation kits were
222 obtained from Thermo Scientific.

223 *Plasmids*

224 All ADR1, spectrin and titin constructs fused to the *E. coli* SecM AP via a variable
225 linker were expressed from the pET19b vector, as described previously (13, 14,

226 20). The spectrin constructs used in this study lacked the soluble domain of LepB
227 at the N-terminus.

228 *Strains and antisera*

229 Strains HDB140 (referred to as WT), HDB143 (referred to as uL23 Δloop) and
230 HDB144 (referred to as uL24 Δloop), as well as rabbit polyclonal antisera against
231 uL23 and uL24, are described in (23).

232 *Isolation of ribosomes*

233 Ribosomes were purified from the strains HDB140, HDB143, and HDB144. The
234 strains were cultured in Lysogeny broth (LB) to an A_{600} of 1.0 at 37°C and chilled
235 on ice for 15 min before they were harvested by centrifugation at 4000 g for 10
236 min. The cell pellet was washed twice with Buffer A at pH 7.5 (10 mM Tris-OAc,
237 14 mM $Mg(OAc)_2$, 60 mM KOAc, 1 mM DTT, 0.1% Complete Protease Inhibitor)
238 and lysed using the Emulsifex (Avestin) at a pressure of 8000 psi. The cell lysate
239 was loaded on a sucrose cushion at pH 7.5 (50 mM Tris-OAc, 1 M KOAc, 15 mM
240 $Mg(OAc)_2$, 1.44 M Sucrose, 1 mM DTT, 0.1% Complete Protease Inhibitor) and
241 centrifuged at 80,000xg in a Ti70 rotor (Beckman-Coulter) for 17 hours. The
242 obtained ribosomal pellet was resuspended in Buffer B at pH 7.5 (50 mM Tris-
243 OAc, 50 mM KOAc, 5 mM $Mg(OAc)_2$, 1 mM DTT), flask frozen in liquid nitrogen
244 and stored at -80°C. This suspension of ribosomes is presumed to consist of a
245 pool of non-translating 30S, 50S and 70S particles due to the concentration of
246 Mg^{2+} in the buffer they are in. Each batch of ribosomes that was prepared was
247 tested for optimal translation by titrating different volumes in the PURExpress®
248 Δ-Ribosome kit.

249 *In vitro transcription and translation*

250 The generated constructs were translated for 20 min. in the PURExpress® Δ-
251 Ribosome kit supplemented with high-salt-washed ribosomes isolated from
252 HDB140, HDB143 (uL23 Δloop), or HDB144 (uL24 Δloop). Plasmid DNA of each
253 construct (300 ng) was used as a template for polypeptide synthesis, and
254 translation was carried out in the presence of (^{35}S) Methionine at 37°C for 20
255 min and shaking at 500 r.p.m. For ADR1a constructs, the translation reactions
256 also included either 50 μM $ZnCl_2$ or 50 μM of the Zn^{2+} chelator TPEN. Translation
257 was stopped by treating the sample with a final concentration of 5%
258 trichloroacetic acid (TCA) and incubated on ice for 30 min. The TCA precipitated
259 samples were subsequently centrifuged at 20,000 g for 10 min in a tabletop
260 centrifuge (Eppendorf) and the pellet obtained was solubilized in sample buffer,
261 supplemented with RNaseA (400 μg/ml), and incubated at 37°C for 15 minutes.
262 The samples were resolved on 12% Bis-Tris gels (Thermo Scientific) in MOPS
263 buffer for ADR1 and MES buffer for Spectrin and Titin. Gels were dried and
264 subjected to autoradiography and scanned using the Fujifilm FLA-9000
265 phosphorimager for visualization of radioactively labeled translated proteins.

266 *Quantification of radioactively labelled proteins*

267 The protein bands on the gel were quantified using MultiGauge (Fujifilm) from
268 which one-dimensional intensity profiles of each gel lane was extracted. This
269 information was subsequently fit to a Gaussian distribution using EasyQuant
270 (Rickard Hedman, Stockholm University). The sum of the arrested and full-length
271 bands was calculated, and this was used to estimate the fraction full-length
272 protein for each construct.

273 *Cryo-EM sample preparation and data processing*

274 The uL23 Δloop ribosomes (4 A_{260}/ml) diluted in grid buffer (20 mM HEPES-
275 KOH, 50 mM KOAc, 10 mM $Mg(OAc)_2$, 125 mM sucrose, 2 mM Trp, 0.03% DDM)
276 were loaded on Pelco® TEM 400 mesh Cu grids pre-coated with 2 nm thick
277 carbon and frozen using the Vitrobot Mark IV (FEI). Data was collected on the
278 Titan Krios (FEI) microscope operated at 300 keV and equipped with a Falcon II
279 direct electron detector. The camera was set to a nominal magnification of
280 75,000X, which resulted in a pixel size of 1.09 Å at the sample level and a defocus
281 range of -1 to -3 µm.

282 The frame dose used was 1.17 e/$Å^2$, and 20 frames were aligned using
283 MotionCor2 (33) within the Scipion software suite (34). The micrographs were
284 visually inspected and those within a resolution threshold of 5 Å were selected,
285 yielding 3522 micrographs.

286 471272 particles were picked using Xmipp manual-pick followed by particle
287 extraction within Scipion and further processing in CryoSPARC (35). Two rounds
288 of 2D classification were done, and particles resembling 30S and 50S subunits
289 alone were discarded after visual inspection of the classes. The remaining
290 297,363 particles of the 70S ribosome were subjected to *ab initio* reconstruction
291 into 3 classes to further sort out heterogeneity. A single homogeneous class
292 consisting of 132,029 particles was used for final homogeneous refinement that
293 resulted in a final map with an average FSC resolution at 0.143 of 3.28 Å. The
294 obtained map of the 70S ribosome was sharpened and corrected for handedness
295 in CryoSPARC fitted with PDBs 3JBU and 4YBB in Chimera (36). Local resolution

296 and FSC at 0.143 was estimated in cryoSPARC. The electron microscopy map was
297 deposited in the Electron Microscopy Data Bank.

298 The initial model for uL23 Δloop was built with Coot, and improved by energy
299 minimization in a solvated dodecahedron box of explicit TIP3P waters,
300 neutralized with chloride ions and using the Amber 99SB-ILDN force field (37).
301 The steepest descent minimization method implemented in GROMACS 2016.1
302 was used (38) (39). Even after minimization, the backbone of the new loop
303 formed after the deletion of residues 65-74 still showed improper geometry and
304 Ramachandran outliers, so we used kinematic sampling (40) to model
305 alternative loop conformations, and then we selected the loop that could fit the
306 electron density and had the best Ramachandran score.

307 Figures were prepared using MacPymol 1.8.6.2 (Schrödinger LLC), Chimera (36),
308 and ChimeraX (41).

309 *Calculation of tunnel volume*

310 The volume calculations were performed with POVME 2.0 (1). We used the *E. coli*
311 SecM structure PDB 3JBU as our reference. To determine the inclusion region, we
312 generated a series of overlapping spheres- eight with a 20 Å radius, and one with
313 a 40 Å radius. In order to have a complete coverage of the exit tunnel, the centers
314 of the spheres were chosen to match the coordinates corresponding to
315 alternating Cα atoms of the amino acids of the SecM arrest peptide located within
316 the exit tunnel (for the 20 Å radius spheres the residues use as centers were D11,
317 F13, T15, V17, I19, Q21, Q23, I25, A27, G28 and for the 40 Å radius sphere the
318 residue was E3). Grid Spacing was set to 2.0 Å, and the distance cut-off to 1.09 Å.
319 For all three cases (WT, uL24 Δ loop, uL23 Δ loop), we used the same inclusion

region. We also removed the SecM arrest peptide located within the exit tunnel. For uL23 Δloop ribosomes residues 65-75 were removed from uL23, and for uL24 Δloop ribosomes residues 42-57 were removed from uL24 (numbering based on PDB 3JBU) prior to the calculation.

Kinetic model to calculate fraction full length protein $f_{FL}(t)$

The theoretical force profiles (Fig. 3d-f) for ADR1a, I27, and R16 were calculated based on a kinetic model introduced in our previous study (20). Briefly, the rate, k_e, of the arrest peptide sequence escape from the peptidyl transfer center with a force (F) exerted by the folding protein can be calculated using the Bell model:

$$k_e(F) = k_0 e^{F\Delta x^{\ddagger}/k_B T},$$

where $\Delta x^{\ddagger}$ is the distance from the free energy minimum to the transition state, k_0 the rupture rate when force equals to zero, k_B is Boltzmann's constant, and T the absolute temperature. In this study, k_0 and $\Delta x^{\ddagger}$ are set to be 3.4 ×10^{-4} s^{-1} and 4.5 Å, respectively, based on a previous experimental study (18) in which k_0 and $\Delta x^{\ddagger}$ were estimated to be in the range of 0.5 ×10^{-4} to 20 ×10^{-4} s^{-1} and 1-8 Å, respectively.

We assume that the folding and unfolding of the protein is much faster than the escape from the ribosome. Then the time-dependent force profile $f_{FL}(t)$ can be obtained approximately by the mean pulling forces exerted when the protein is unfolded, F_u, or folded, F_f, and the unfolded and folded populations of P_u and P_f respectively,

$$f_{FL}(t) \approx 1 - \exp\left[-t\left[P_u k_e(F_u) + P_f k_e(F_f)\right]\right].$$

342 Note that the values of F_u, F_f , P_u, P_f are dependent on the linker length *L*, and can
343 be determined by molecular dynamics simulations.

344 *Molecular dynamics simulations of ribosome-nascent chain complex*

345 A coarse-grained model was employed to simulate folding of ADR1a, I27, and
346 R16 on the ribosome. The ribosome was modelled on the 50S subunit of the *E.*
347 *coli* ribosome (PDB 3OFR; (42)) Each amino acid in the nascent chain and
348 ribosome was represented by one bead at the position of the α-carbon atom,
349 each RNA residue was modelled by three beads which represent phosphate P,
350 sugar C4', and base N3 (43). The uL23 Δloop ribosome was modelled by
351 replacing the coordinates of the wildtype uL23 protein with the cryo-EM
352 structure of the uL23 Δloop protein from this study (PDB 6FU8), after being
353 aligned to the wild type protein. The uL24 Δloop ribosome was modelled by
354 replacing the coordinates of the wildtype uL24 protein with the structure of the
355 uL24 Δloop protein built by homology modelling with Modeller (44).

356 The interactions within the nascent chain were governed by a standard
357 structure-based model (45), which allowed it to reversibly fold to the native
358 state and unfold. Interactions between the protein and ribosome beads were
359 purely repulsive. The pulling force (F) exerted on the arrest peptide by the
360 folding of the protein (ADR1a, R16, or I27) was measured by the extension of the
361 harmonic pseudobond potential between the last and the second last amino acid
362 of the SecM arrest peptide. More details can be found in our previous study (20).

363

364 **References**

365 1. Milligan RA & Unwin PN (1986) Location of exit channel for nascent
366 protein in 80S ribosome. *Nature* 319:693-695.
367 2. Ban N, Nissen P, Hansen J, Moore PB, & Steitz TA (2000) The complete
368 atomic structure of the large ribosomal subunit at 2.4 A resolution.
369 *Science* 289:905-920.
370 3. Nissen P, Hansen J, Ban N, Moore PB, & Steitz TA (2000) The structural
371 basis of ribosome activity in peptide bond synthesis. *Science* 289:920-930.
372 4. Klein DJ, Moore PB, & Steitz TA (2004) The roles of ribosomal proteins in
373 the structure assembly, and evolution of the large ribosomal subunit. *J*
374 *Mol Biol* 340:141-177.
375 5. Lawrence MG*, et al.* (2016) The extended loops of ribosomal proteins uL4
376 and uL22 of Escherichia coli contribute to ribosome assembly and protein
377 translation. *Nucleic Acids Res* 44:5798-5810.
378 6. Nissen P, Hansen J, Ban N, Moore P, & Steitz T (2000) The structural basis
379 of ribosome activity in protein synthesis. *Science* 289:920-930.
380 7. Harms J*, et al.* (2001) High resolution structure of the large ribosomal
381 subunit from a mesophilic eubacterium. *Cell* 107:679-688.
382 8. O'Brien EP, Hsu ST, Christodoulou J, Vendruscolo M, & Dobson CM (2010)
383 Transient tertiary structure formation within the ribosome exit port. *J Am*
384 *Chem Soc* 132:16928-16937.
385 9. O'Brien EP, Christodoulou J, Vendruscolo M, & Dobson CM (2011) New
386 scenarios of protein folding can occur on the ribosome. *J Am Chem Soc*
387 133:513-526.

388 10. Trovato F & O'Brien EP (2016) Insights into Cotranslational Nascent
389 Protein Behavior from Computer Simulations. *Annu Rev Biophys* 45:345-
390 369.
391 11. Farias-Rico JA, Ruud Selin F, Myronidi I, Frühauf M, & von Heijne G (2018)
392 Effects of protein size, thermodynamic stability, and net charge on
393 cotranslational folding on the ribosome. *Proc Natl Acad Sci U S A* in press.
394 12. Samelson AJ*, et al.* (2018) Kinetic and structural comparison of a protein's
395 cotranslational folding and refolding pathways. *Sci Adv* 4:eaas9098.
396 13. Nilsson OB*, et al.* (2015) Cotranslational protein folding inside the
397 ribosome exit tunnel. *Cell reports* 12:1533-1540.
398 14. Nilsson OB*, et al.* (2017) Cotranslational folding of spectrin domains via
399 partially structured states. *Nat Struct Mol Biol* 24:221-225.
400 15. Nakatogawa H & Ito K (2001) Secretion monitor, SecM, undergoes self-
401 translation arrest in the cytosol. *Mol Cell* 7:185-192.
402 16. Ismail N, Hedman R, Lindén M, & von Heijne G (2015) Charge-driven
403 dynamics of nascent-chain movement through the SecYEG translocon. *Nat*
404 *Struct Mol Biol* 22:145-149.
405 17. Ismail N, Hedman R, Schiller N, & von Heijne G (2012) A biphasic pulling
406 force acts on transmembrane helices during translocon-mediated
407 membrane integration. *Nature Struct Molec Biol* 19:1018-1022.
408 18. Goldman DH*, et al.* (2015) Mechanical force releases nascent chain-
409 mediated ribosome arrest *in vitro* and *in vivo*. *Science* 348:457-460.
410 19. Shimizu Y, Kanamori T, & Ueda T (2005) Protein synthesis by pure
411 translation systems. *Methods* 36:299-304.

412 20. Tian P, *et al.* (2018) The folding pathway of an Ig domain is conserved on
413 and off the ribosome. *BioRxiv* doi: https://doi.org/10.1101/253013.
414 21. Farias-Rico JA, Goetz SK, Marino J, & von Heijne G (2017) Mutational
415 analysis of protein folding inside the ribosome exit tunnel. *FEBS Lett*
416 591:155-163.
417 22. Notari L, Martinez-Carranza M, Farias-Rico JA, Stenmark P, & von Heijne G
418 (2018) Cotranslational folding of a pentarepeat β-helix protein. *bioRxiv*
419 https://doi.org/10.1101/255810.
420 23. Peterson JH, Woolhead CA, & Bernstein HD (2010) The conformation of a
421 nascent polypeptide inside the ribosome tunnel affects protein targeting
422 and protein folding. *Mol Microbiol* 78:203-217.
423 24. Bubunenko MG, Schmidt J, & Subramanian AR (1994) Protein substitution
424 in chloroplast ribosome evolution. A eukaryotic cytosolic protein has
425 replaced its organelle homologue (L23) in spinach. *J Mol Biol* 240:28-41.
426 25. Bieri P, Leibundgut M, Saurer M, Boehringer D, & Ban N (2017) The
427 complete structure of the chloroplast 70S ribosome in complex with
428 translation factor pY. *EMBO J* 36:475-486.
429 26. Durrant JD, de Oliveira CA, & McCammon JA (2011) POVME: an algorithm
430 for measuring binding-pocket volumes. *J Mol Graph Model* 29:773-776.
431 27. Durrant JD, Votapka L, Sorensen J, & Amaro RE (2014) POVME 2.0: An
432 Enhanced Tool for Determining Pocket Shape and Volume Characteristics.
433 *J Chem Theory Comput* 10:5047-5056.
434 28. Capece MC, Kornberg GL, Petrov A, & Puglisi JD (2015) A simple real-time
435 assay for in vitro translation. *RNA* 21:296-305.

436 29. Wilson DN & Doudna Cate JH (2012) The structure and function of the
437 eukaryotic ribosome. *Cold Spring Harb Perspect Biol* 4.
438 30. Filipovska A & Rackham O (2013) Specialization from synthesis: how
439 ribosome diversity can customize protein function. *FEBS Lett* 587:1189-
440 1197.
441 31. Melnikov S, Ben-Shem A, Yusupova G, & Yusupov M (2015) Insights into
442 the origin of the nuclear localization signals in conserved ribosomal
443 proteins. *Nat Commun* 6:7382.
444 32. Schiller N, Magoulopoulou A, Cymer F, & von Heijne G (2017) Mutational
445 analysis of the human Xbp1 translational arrest peptide and construction
446 of arrest-enhanced variants. *bioRxiv* https://doi.org/10.1101/201913.
447 33. Li X, *et al.* (2013) Electron counting and beam-induced motion correction
448 enable near-atomic-resolution single-particle cryo-EM. *Nat Methods*
449 10:584-590.
450 34. de la Rosa-Trevin JM, *et al.* (2016) Scipion: A software framework toward
451 integration, reproducibility and validation in 3D electron microscopy.
452 *Journal of structural biology* 195:93-99.
453 35. Punjani A, Rubinstein JL, Fleet DJ, & Brubaker MA (2017) cryoSPARC:
454 algorithms for rapid unsupervised cryo-EM structure determination. *Nat*
455 *Methods* 14:290-296.
456 36. Pettersen EF, *et al.* (2004) UCSF Chimera--a visualization system for
457 exploratory research and analysis. *Journal of computational chemistry*
458 25:1605-1612.
459 37. Lindorff-Larsen K, *et al.* (2010) Improved side-chain torsion potentials for
460 the Amber ff99SB protein force field. *Proteins* 78:1950-1958.

461 38. Abraham M, *et al.* (2015) GROMACS: High performance molecular
462 simulations through multi-level parallelism from laptops to
463 supercomputers. *SoftwareX* 1:19-25.
464 39. Pal S, Abraham MJ, Kutzner C, Hess B, & Lindahl E (2014) *Solving software*
465 *challenges for exascale* (Springer, Cham, Switzerland).
466 40. Bhardwaj G, *et al.* (2016) Accurate de novo design of hyperstable
467 constrained peptides. *Nature* 538:329-335.
468 41. Goddard TD, *et al.* (2018) UCSF ChimeraX: Meeting modern challenges in
469 visualization and analysis. *Protein Sci* 27:14-25.
470 42. Dunkle JA, Xiong L, Mankin AS, & Cate JH (2010) Structures of the
471 Escherichia coli ribosome with antibiotics bound near the peptidyl
472 transferase center explain spectra of drug action. *Proc Natl Acad Sci U S A*
473 107:17152-17157.
474 43. Voss NR & Gerstein M (2005) Calculation of standard atomic volumes for
475 RNA and comparison with proteins: RNA is packed more tightly. *J Mol Biol*
476 346:477-492.
477 44. Eswar N, *et al.* (2006) Comparative protein structure modeling using
478 Modeller. *Curr Protoc Bioinformatics* Chapter 5:Unit-5 6.
479 45. Karanicolas J & Brooks CL, 3rd (2002) The origins of asymmetry in the
480 folding transition states of protein L and protein G. *Protein Sci* 11:2351-
481 2361.
482 46. Zhang J, *et al.* (2015) Mechanisms of ribosome stalling by SecM at multiple
483 elongation steps. *eLife* DOI 10.7554/eLife.09684.
484
485

487 **Figure legends**

488 *Figure 1*. (A) Front view of the 50S subunit of the *E. coli* ribosome adapted from
489 PDB 3JBU (46), with tunnel proteins uL4 and uL22 indicated in gray. The
490 globular domain of uL23 is indicated in orange with the β-hairpin loop depicted
491 in yellow. uL24 is shown in dark blue, with the loop at the tunnel exit shown in
492 light blue. The exit tunnel, outlined by a stalled SecM nascent chain (purple), is
493 ~100 Å in length. (B) The arrest-peptide assay (13). The domain to be studied is
494 placed *L* residues upstream of the critical proline at the C-terminal end of the 17-
495 residue long arrest peptide (AP) from the *E. coli* SecM protein. A 23-residue long
496 stretch of the *E. coli* LepB protein is attached downstream of the AP, allowing us
497 to separate the arrested (A) and full-length (FL) products by SDS-PAGE after
498 translation. Constructs are translated in the PURExpress® *in vitro* translation
499 system supplemented with WT, uL23 Δloop, or uL24 Δloop high-salt washed
500 ribosomes for 20 min. The relative amounts of arrested and full-length protein
501 were estimated by quantification of SDS-PAGE gels, and the fraction of full-length
502 protein was calculated as $f_{FL} = I_{FL}/(I_A + I_{FL})$ where I_A and I_{FL} are the intensities of
503 the bands corresponding to the A and FL products. (c) f_{FL} is a proxy for the force
504 F that cotranslational folding of a protein domain exerts on the AP. At short
505 linker lengths, both F and $f_{FL} \approx 0$ because the domain is unable to fold due to lack
506 of space in the exit tunnel. At intermediate linker lengths, F and $f_{FL} > 0$ because
507 the domain pulls on the nascent chain as it folds. At longer linker lengths, F and
508 $f_{FL} \approx 0$ because the domain is already folded when the ribosome reaches the end
509 of the AP.

510 **Figure 1- figure supplement 1**. A_{260} = 300 units (6.9 μM**)** of high-salt washed
511 ribosomes were separated on a 12% Bis-Tris gel and transferred by Western
512 blotting onto a nitrocellulose membrane and detected with antibodies against
513 uL24 (panel A) or uL23 (panel B).

514 **Figure 1- figure supplement 2.** Multiple sequence alignment of uL23 (A) and
515 uL24 (B). The uL23 and uL24 b-hairpin loops, boxed, respectively, in orange and
516 blue, are conserved among Gram-negative bacteria, but are short or absent in
517 archaea and eukaryotes. In eukaryotes and archaea, part of the function of uL23
518 is proposed to be fulfilled by ribosomal protein eL39.

519

520 ***Figure 2***. Structural consequences of removing the hairpin loops in uL24 and
521 uL23 modeled after PDB 3JBU of the SecM stalled ribosome. (A) In wildtype
522 ribosomes, the loop in uL24 partially obstructs the exit tunnel (top panel). Its
523 removal in uL24 Δloop ribosomes creates a wide opening into the tunnel
524 (bottom panel). (B) In wildtype ribosomes, the loop in uL23 extends into the exit
525 tunnel (top panel). Its removal in uL23 Δloop ribosomes creates an open space
526 around the area where the ADR1a domain is known to fold (13). The ADR1a
527 structure is from PDB 5A7U. (C) Cryo-EM structure of the uL23 Δloop 70 S
528 ribosome (EMD-4319), fitted to PDB 3JBU (that includes a Gly-tRNA and a 26-
529 residue long arrested SecM AP) to locate uL23 (orange) and the exit tunnel. The
530 enlarged region shows a difference map (in mesh) obtained by subtracting the
531 cryo-EM map of the uL23 Δloop 70 S ribosome from a map generated from 3JBU
532 in Chimera. The difference map shows that the only difference in volume
533 between the two maps is the tRNA (in pink), the SecM AP (in magenta), and the

534 loop deleted from uL23. (D) Extracted cryo-EM density (in mesh) for uL23 in the
535 uL23 Δloop ribosome EMD-4319. Wildtype uL23 (orange) and a *de novo*-built
536 model for the mutant uL23 Δloop protein (PDB 6FU8; red) are shown in ribbon
537 representation.

538 **Figure 2- figure supplement 1**. Resolution map of the uL23Δ loop ribosome. (A)
539 Calculation of the local resolution using cryoSPARC. (B) Resolution histogram at
540 FSC 0.143. (C) Fourier-Shell correlation (FSC) curve of the refined map at 0.143
541 indicating an average resolution of 3.28 Å.

542

543 ***Figure 3.*** (A) Δf_{FL} profiles ($\Delta f_{FL} = f_{FL}$(50 μM Zn^{2+}) – f_{FL}(50 μM TPEN)) for ADR1a
544 constructs translated in the PURE system supplemented with in-house purified
545 WT (gray), uL23 Δloop (red), and uL24 Δloop (blue) *E. coli* ribosomes. (B) f_{FL}
546 profiles for spectrin R16 constructs translated in the PURE system supplemented
547 with in-house purified WT (gray), uL23 Δloop (red), and uL24 Δloop (blue) *E.*
548 *coli* ribosomes. (C) f_{FL} profiles for titin I27 constructs translated in the PURE
549 system supplemented with in-house purified WT (gray), uL23 Δloop (red), and
550 uL24 Δloop (blue) *E. coli* ribosomes. Error bars in panels a-c show SEM values
551 calculated from at least 3 independent experiments. Dashed lines indicate L_{onset}
552 and L_{end} values, c.f., Table 1. f_{FL} profiles for non-folding mutants of R16 and I27
553 are found in (14, 20). (D) Simulated f_{FL} profiles (full lines) for ADR1a, spectrin
554 R16, and titin I27 obtained with WT (gray), uL23 Δloop (red), and uL24 Δloop
555 (blue) ribosomes. The corresponding experimental f_{FL} profiles from panels a-c
556 are shown as dashed lines. The simulated ADR1a f_{FL} profile marked by X's was

557 obtained with a uL23 Δloop(70-72) ribosome model. Simulated f_{FL} profiles for
558 ADR1a with uL24 Δloop ribosomes, and for R16 and I27 with uL23 Δloop
559 ribosomes, are essentially identical to the corresponding profiles obtained with
560 WT ribosomes, and are shown in Figure 3-figure supplement 10.

561 **Figure 3- figure supplement 1-4.** SDS PAGE showing ADR1 constructs
562 translated in PURExpress® Δ-Ribosome kit supplemented with high-salt-washed
563 ribosomes isolated from HDB140, HDB143 (uL23 Δloop), or HDB144 (uL24
564 Δloop) as indicated. Translations were run on 12% Bis-Tris gels with MOPS
565 running buffer.

566 **Figure 3- figure supplement 5-6.** SDS PAGE showing Spectrin R16 constructs
567 translated in PURExpress® Δ-Ribosome kit supplemented with high-salt-washed
568 ribosomes isolated from HDB140, HDB143 (uL23 Δloop), or HDB144 (uL24
569 Δloop) as indicated. Translations were run on 12% Bis-Tris gels with MES
570 running buffer.

571 **Figure 3- figure supplement 6-7.** SDS PAGE showing Titin I27 constructs
572 translated in PURExpress® Δ-Ribosome kit supplemented with high-salt-washed
573 ribosomes isolated from HDB140, HDB143 (uL23 Δloop), or HDB144 (uL24
574 Δloop) as indicated. Translations were run on 12% Bis-Tris gels with MES
575 running buffer.

576 **Figure 3- figure supplement 8.** f_{FL} profiles for ADR1a constructs translated in
577 PURE by WT, uL23 Δloop, and uL24 Δloop ribosomes, either in the presence of
578 Zn^{2+} or of the Zn^{2+} chelator TPEN. Averages and standard errors calculated from
579 three independent translation reactions are shown.

580

581 **Figure 3- figure supplement 9.** Sequences of the longest and the shortest
582 constructs used for each protein and, a depiction of the location of the sequences
583 the ribosome exit tunnel when the last residue of the AP is in the P-site (lower
584 panel, yellow box). ADR1 is indicated in red, spectrin R16 in blue, titin I27 in
585 pink, and the SecM AP in magenta. The linker between each domain and the AP is
586 in grey. The part of LepB added to the N-terminus of ADR1a is in black**.**

587 **Figure 3- figure supplement 10.** Summary of results from coarse-grained MD
588 simulations. (A) Average forces exerted on the AP by the folded state (first
589 column), fraction folded protein (second column), and f_{FL} values (last column)
590 for ADR1a, I27, and R16 at different linker lengths *L.* (B) Snapshots of folded
591 ADR1a, I27, and R16 domains in wildtype (WT), uL23 Δloop, and uL24 Δloop
592 ribosomes at *L* values ≈ L_{onset}. Note that the folded proteins are located at similar
593 depths in the exit tunnel in the cryo-EM structures and the simulations for WT
594 ribosomes (this holds also for ADR1a in uL24 Δloop ribosomes as well as for I27
595 and R16 in uL23 Dloop ribosomes, c.f. panel A). The C terminus of folded ADR1a
596 is located ~6 Å deeper in the exit tunnel in uL23 Δloop than in WT ribosomes,
597 while folded I27 and R16 are located, respectively, ~15 Å and ~13 Å deeper in
598 the exit tunnel in uL24 Δloop ribosomes (dashed guide lines). Note that the
599 linker is more stretched in the WT ribosome simulations compared to the Δloop
600 ribosomes, consistent with the higher force and lower fraction folded protein
601 seen for the WT ribosome data at the same *L* values (panel a).

602 *Video 1.* The ribosome exit tunnel (mesh), as calculated for PDB 3JBU, uL23 Δloop
603 and uL24 Δloop ribosomes by POVME. See Fig. 1A for coloring scheme. The b-
604 hairpin loops deleted in uL23 Δloop and uL24 Δloop ribosomes are shown in

605 yellow and light blue, respectively. To facilitate the visualization of the exit

606 tunnel, spheres left outside the exit tunnel after POVME processing were

607 manually removed.

608

609 **Table 1**

610 L_{onset}, L_{max}, and L_{end} values calculated from the f_{FL} profiles in Fig. 3.

611

	ADR1a			R16			I27		
	WT	uL23 Δloop	uL24 Δloop	WT	uL23 Δloop	uL24 Δloop	WT	uL23 Δloop	uL24 Δloop
L_{onset}	21	17	20	31	31	29	32	33	28
L_{max}	25	22	25	35	35	33	35	35	35
L_{end}	27	26	27	42	39	40	38	38	41

Figure 1

A

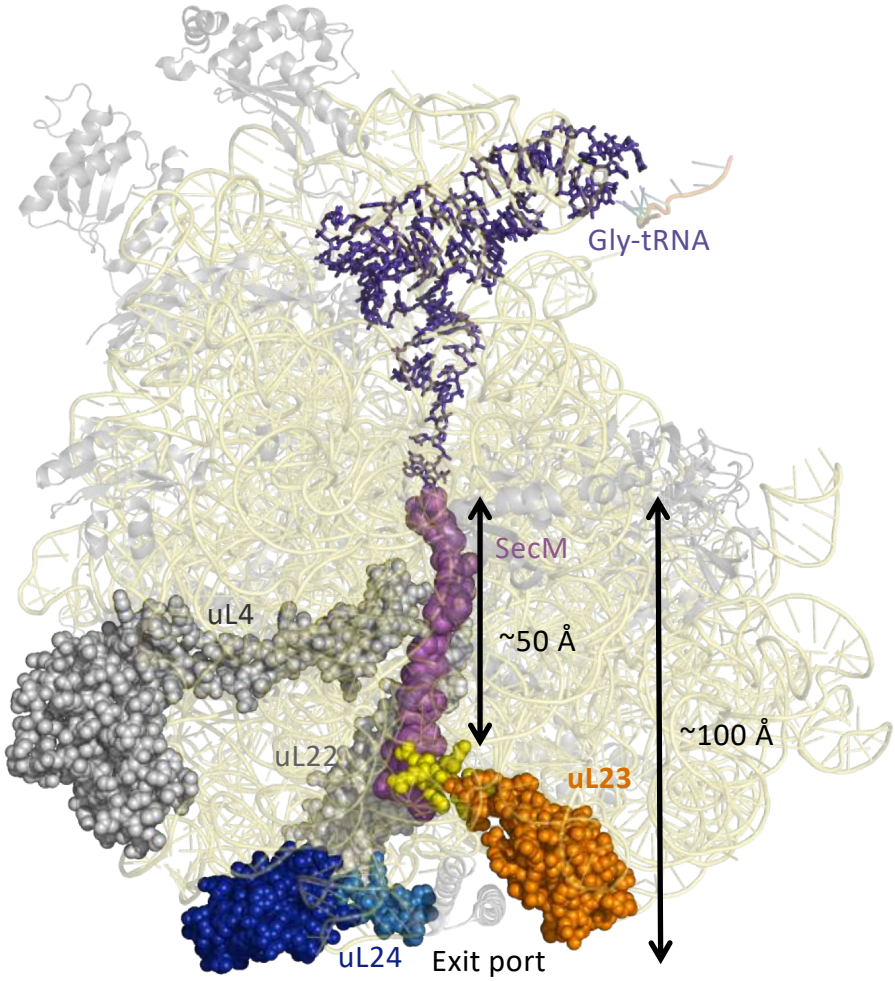
Gly-tRNA
SecM
uL4
~50 Å
~100 Å
uL22
uL23
uL24
Exit port

B

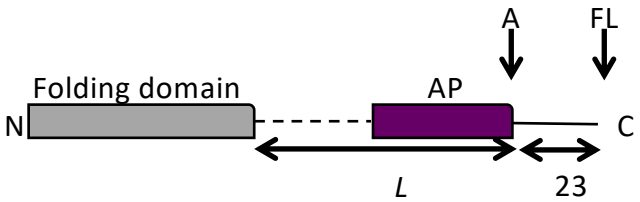
A
FL
Folding domain
AP
N
C
L
23

C

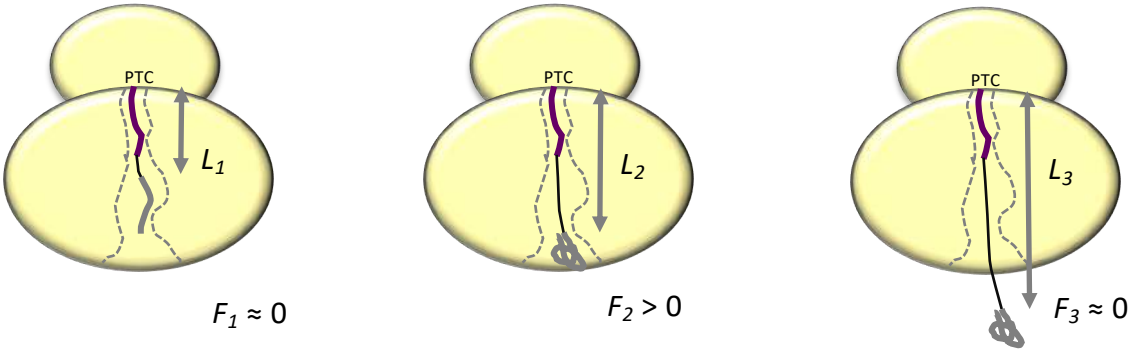
PTC
L_1
$F_1 \approx 0$
PTC
L_2
$F_2 > 0$
PTC
L_3
$F_3 \approx 0$

Figure 1- figure supplement 1

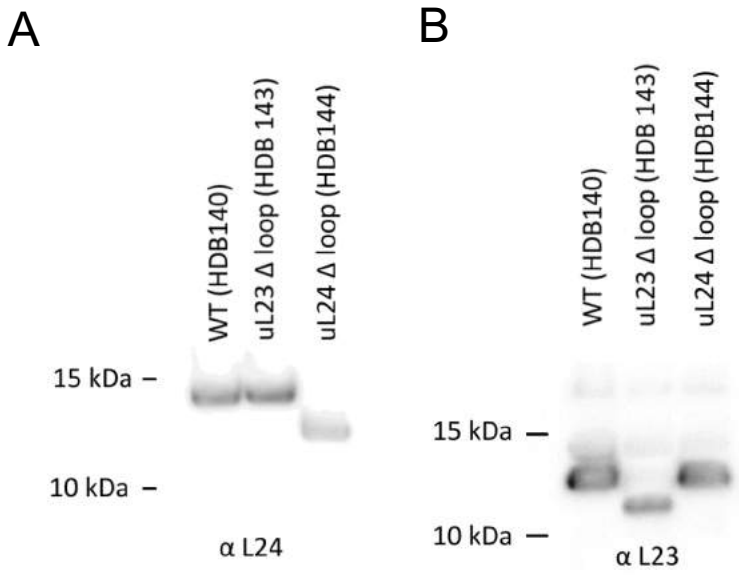

Figure 1- figure supplement 2

A

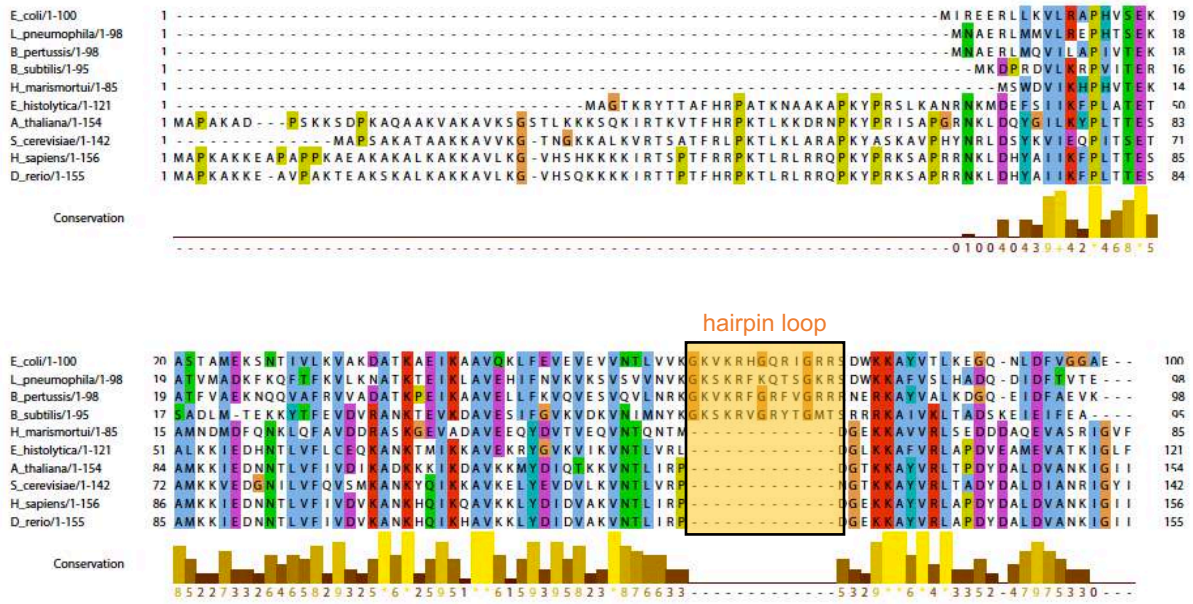

B

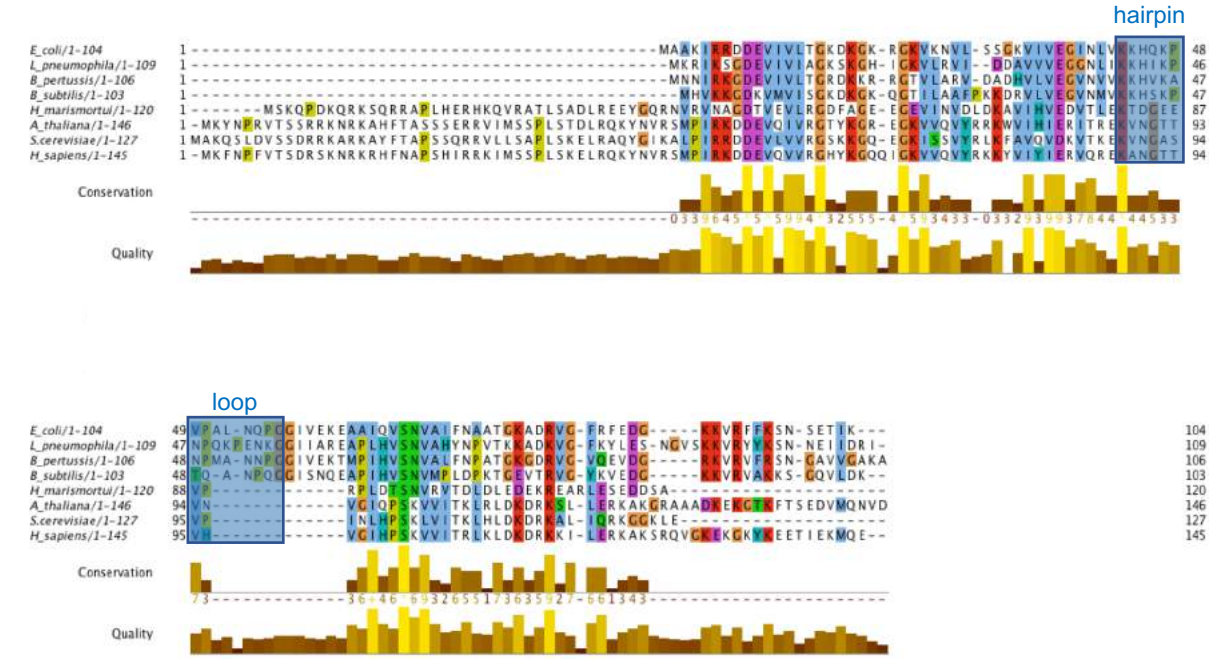

Figure 2

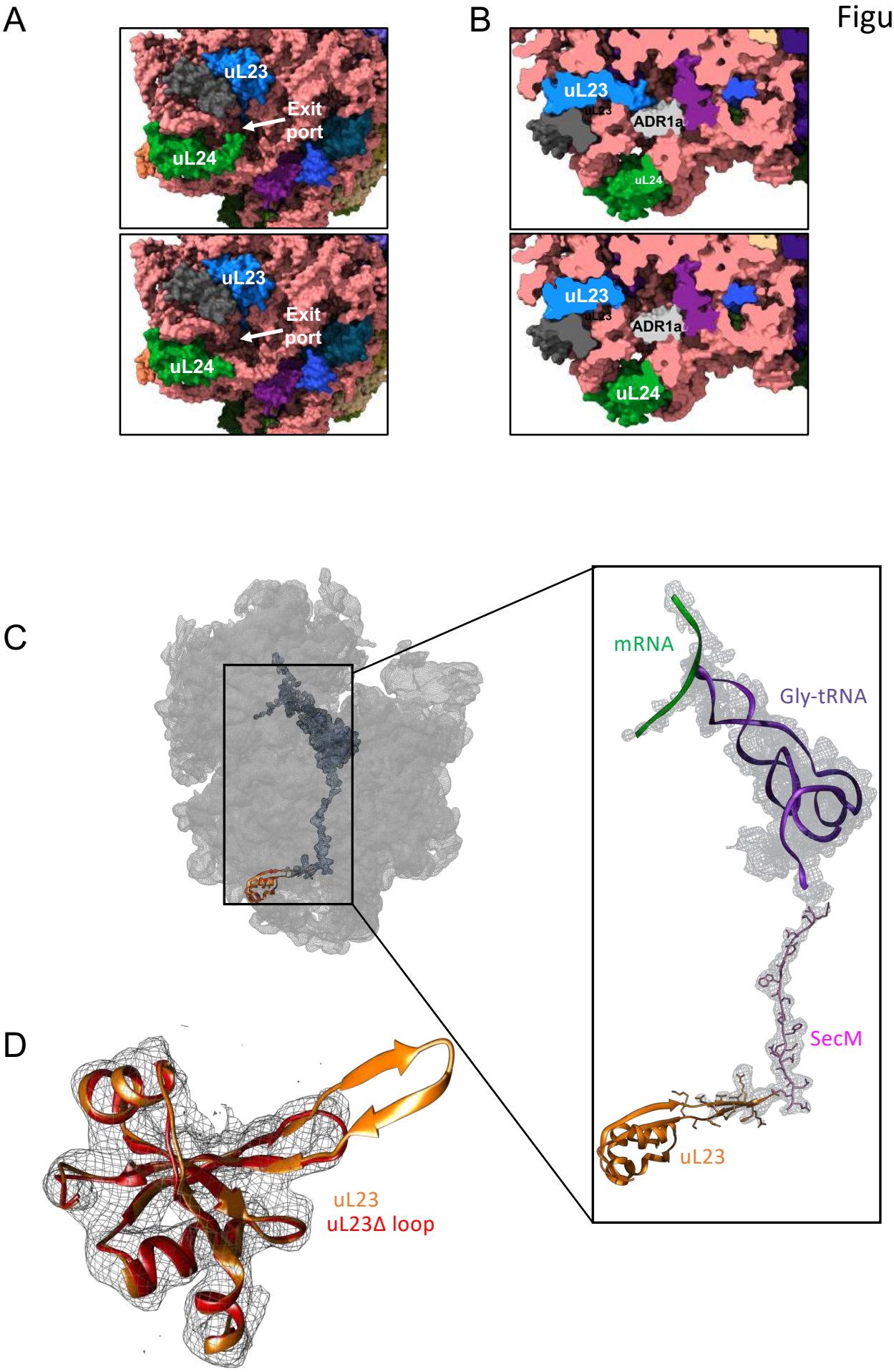
A
uL23
Exit
port
uL24
uL23
Exit
port
uL24
B
uL23
uL23
ADR1a
uL24
uL23
uL23
ADR1a
uL24
C
mRNA
Gly-tRNA
SecM
uL23
D
uL23
uL23Δ loop

Figure 2- figure supplement 1

A

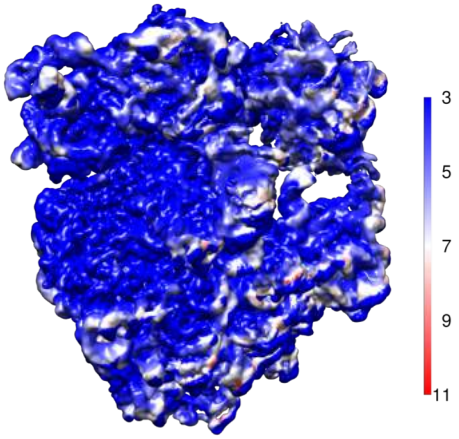

B

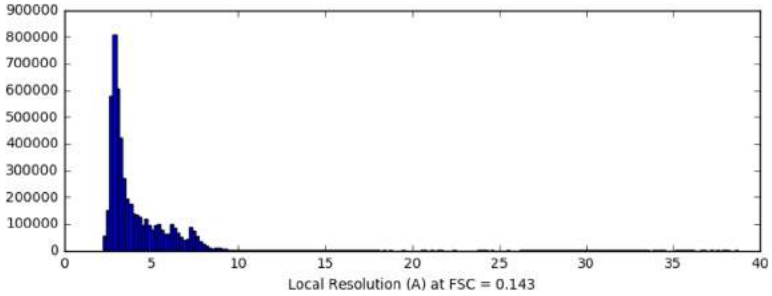

C

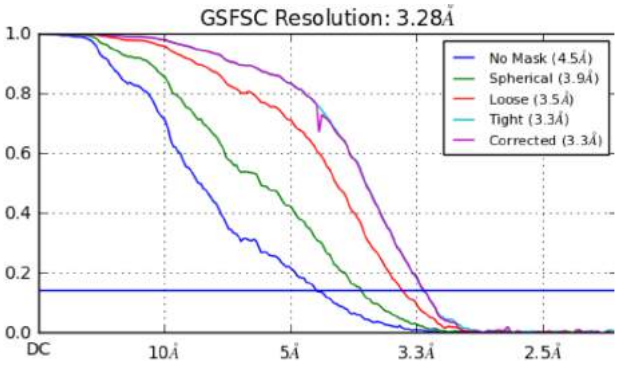

Figure 3

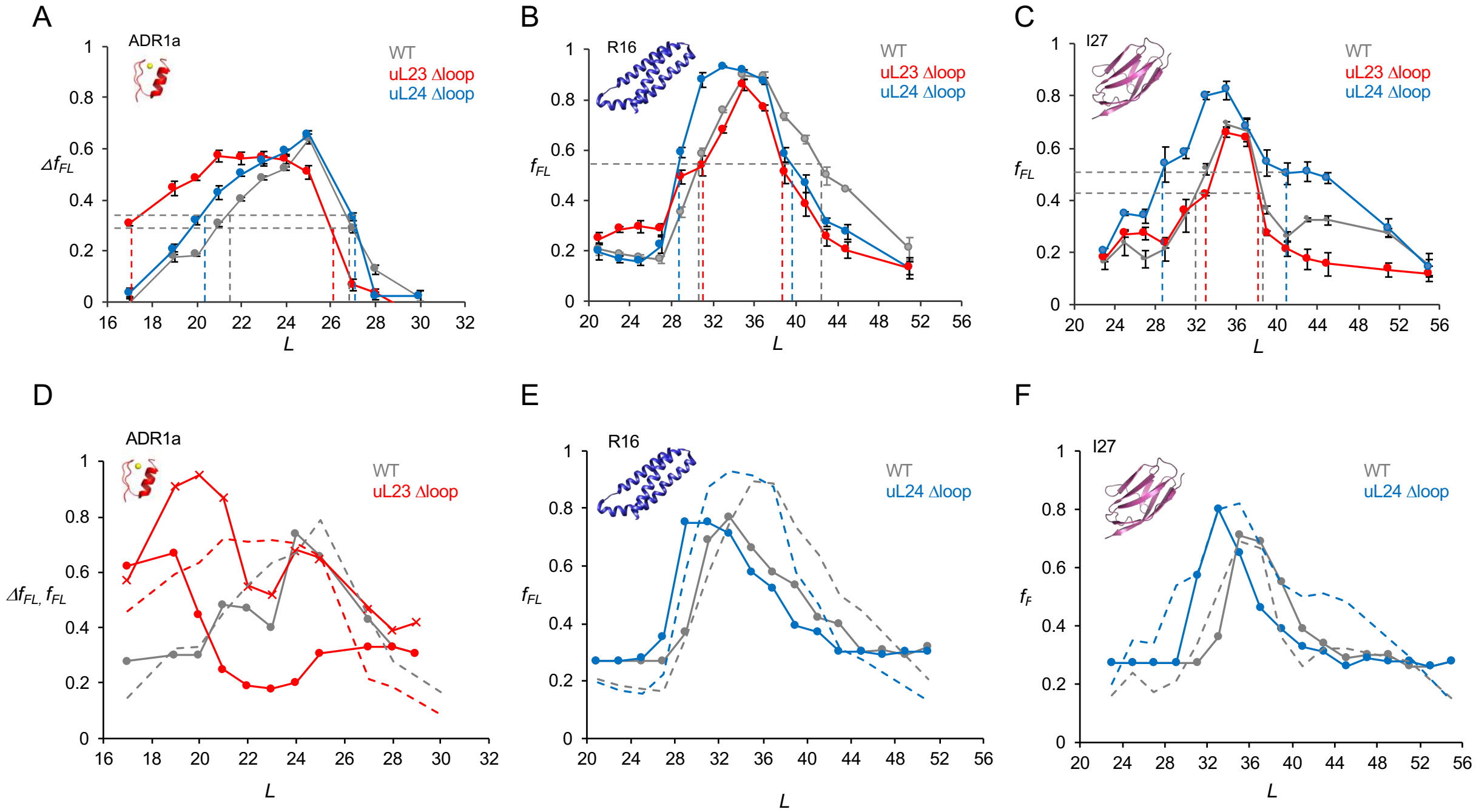
A
ADR1a
WT
uL23 Δloop
uL24 Δloop
Δf_{FL}
L
B
R16
WT
uL23 Δloop
uL24 Δloop
f_{FL}
L
C
I27
WT
uL23 Δloop
uL24 Δloop
f_{FL}
L
D
ADR1a
WT
uL23 Δloop
Δf_{FL}, f_{FL}
L
E
R16
WT
uL24 Δloop
f_{FL}
L
F
I27
WT
uL24 Δloop
L

Figure 3- figure supplement 1

Translation of ADR1a with NEB commercial ribosomes

Single replicate

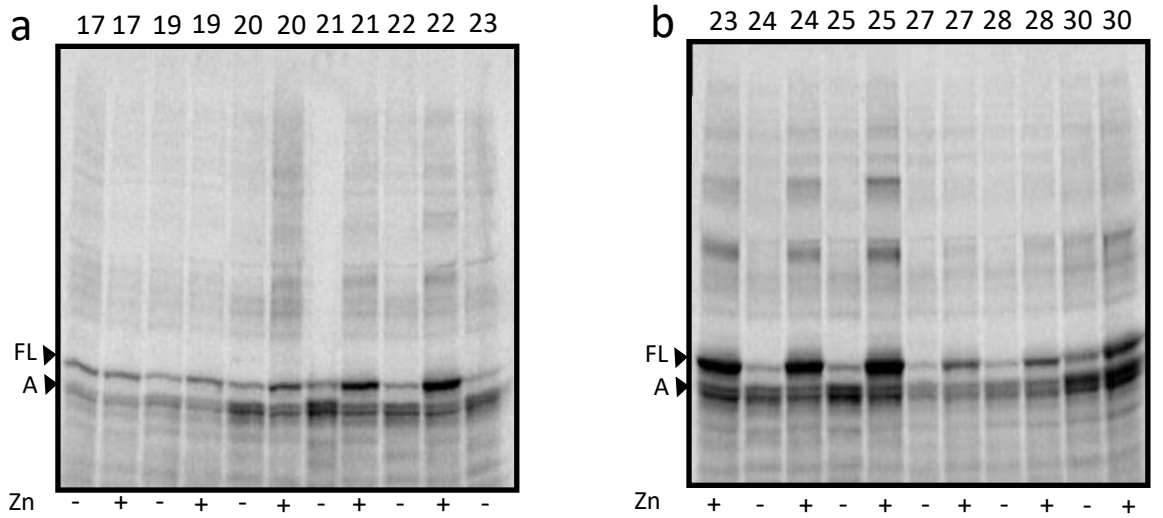

Translation of ADR1a with WT ribosomes from strain HDB140

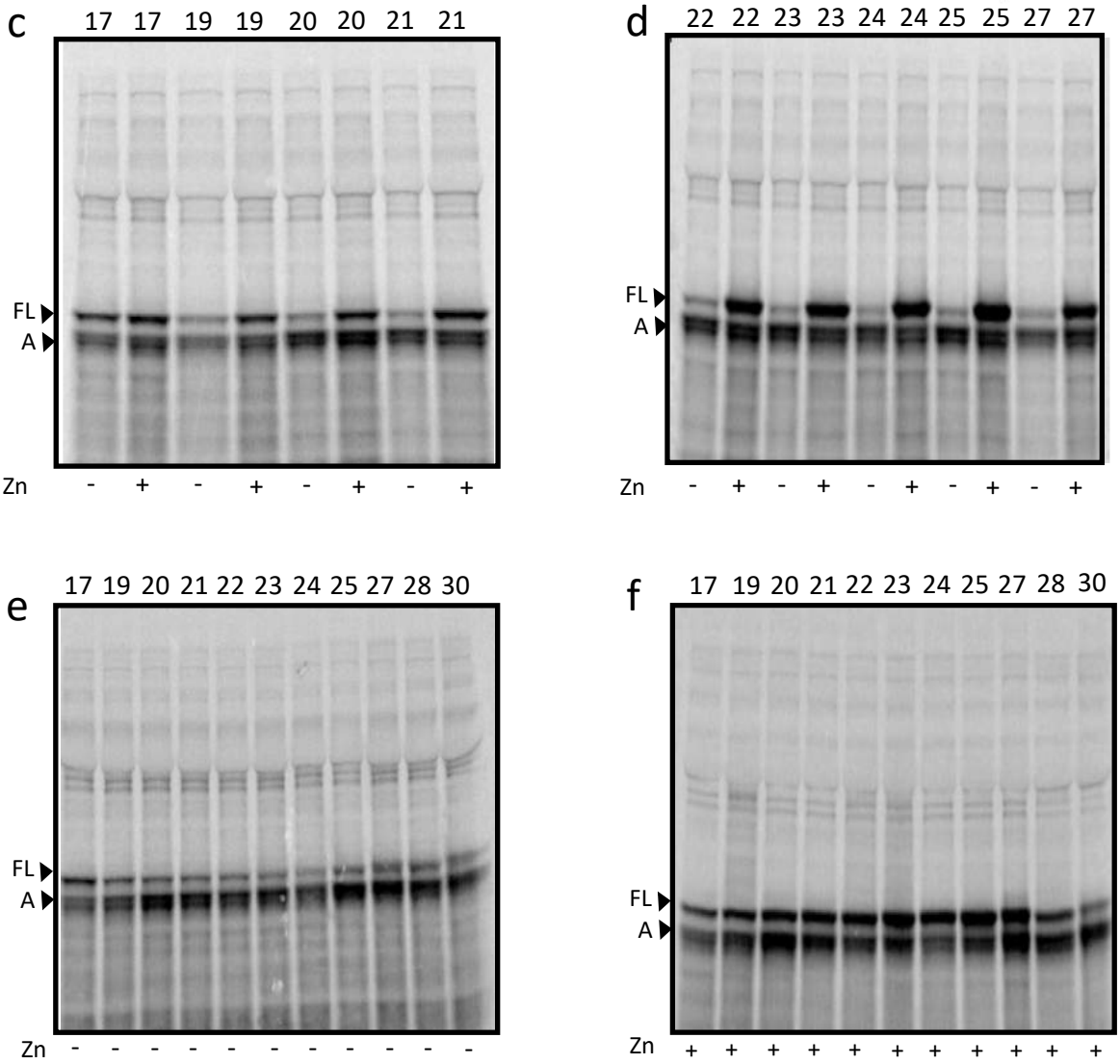

Figure 3- figure supplement 2

Translation of ADR1a with WT ribosomes from strain HDB140 (except gel 'a' lane indicated 24*, see note below gel)

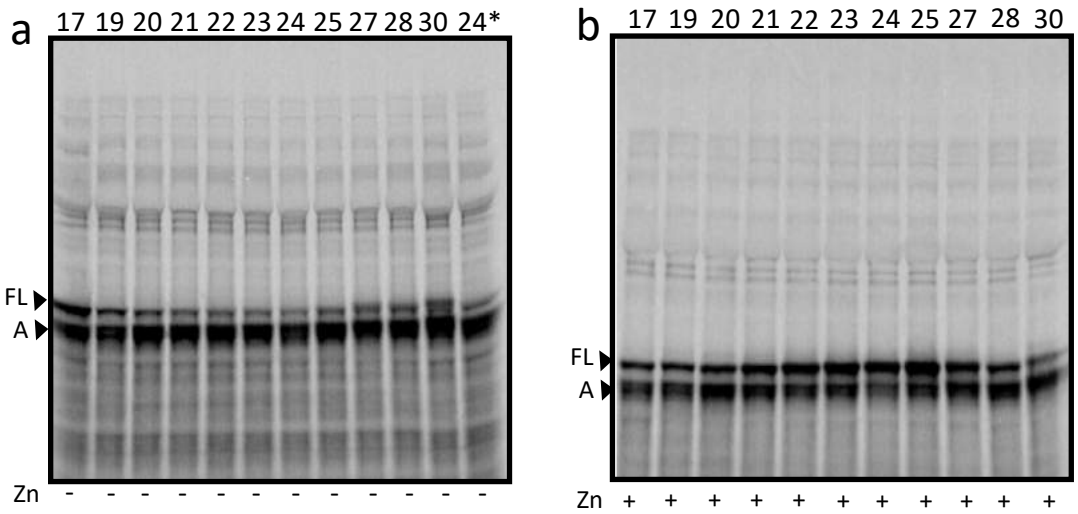

24* = Linker length 24 translated with uL23Δloop ribosomes

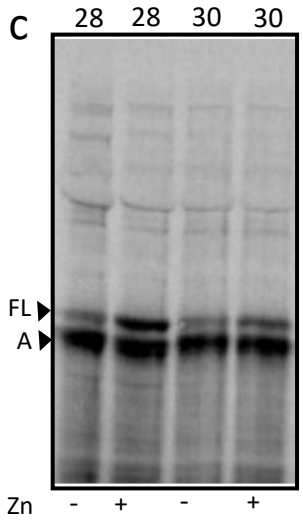

Translation of ADR1a with uL23Δloop ribosomes from strain HDB143

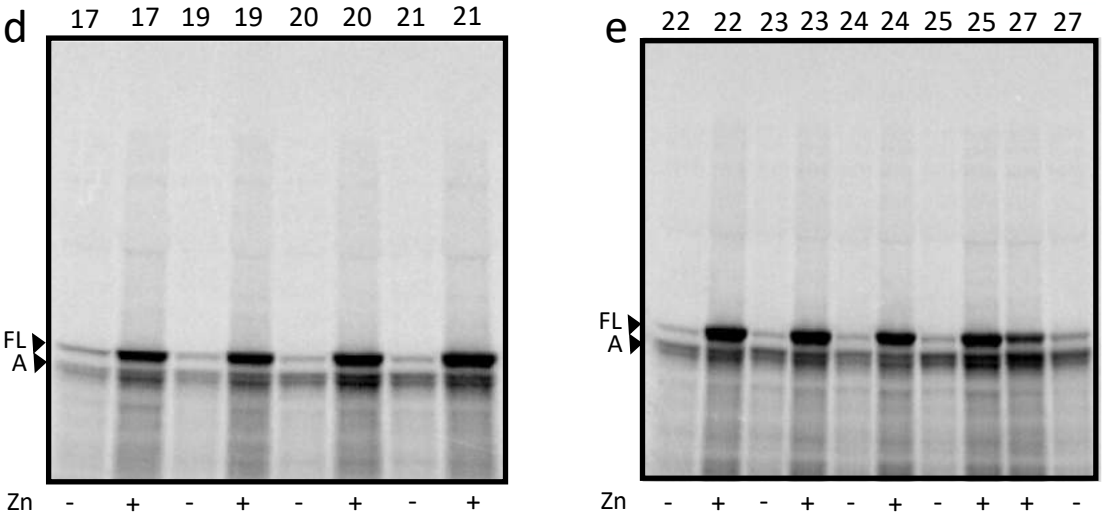

Figure 3- figure supplement 3

Translation of ADR1a with uL23Δloop ribosomes from strain HDB143

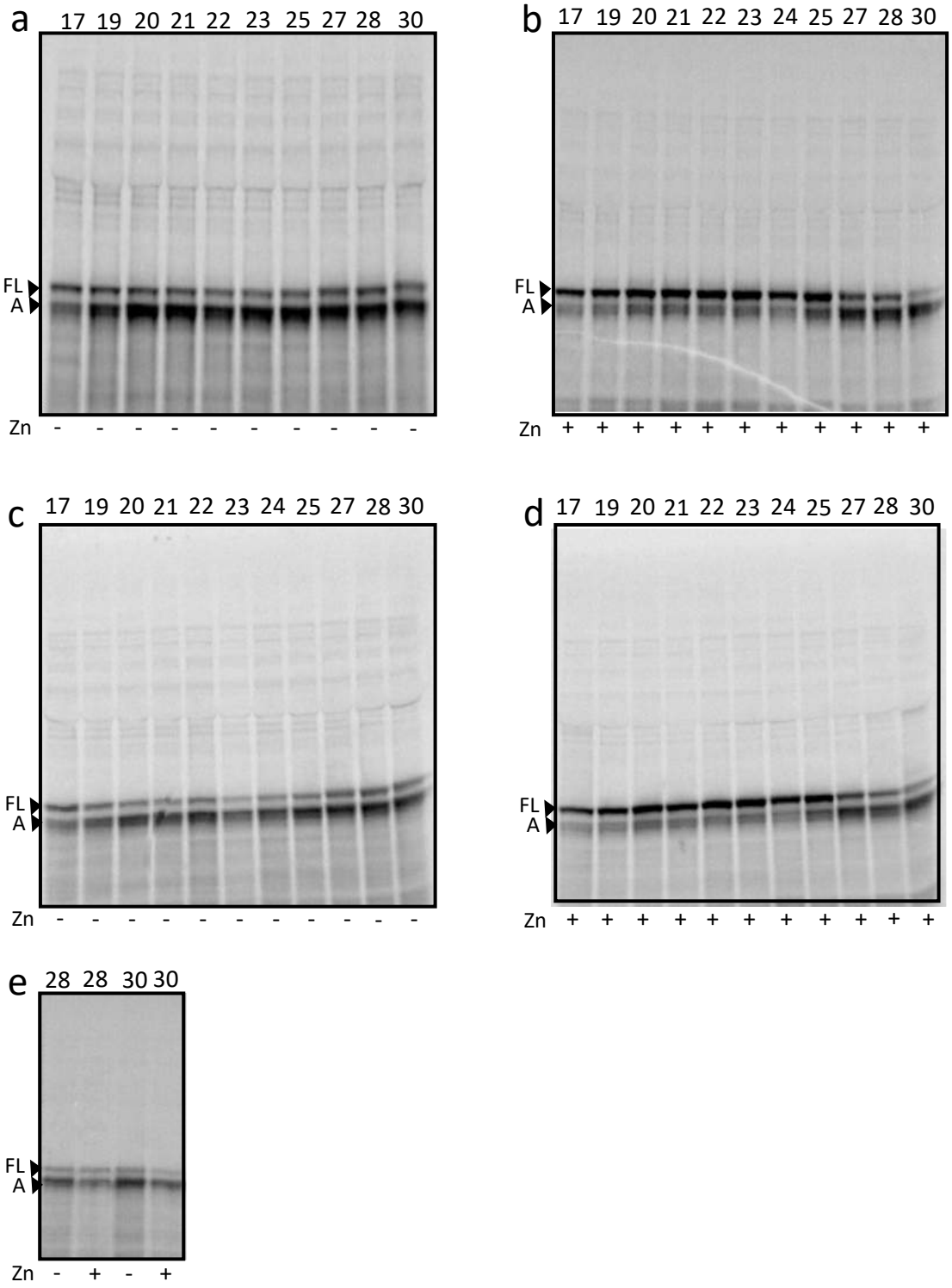

Figure 3- figure supplement 4

Translation of ADR1a with uL24Δloop ribosomes from strain HDB144

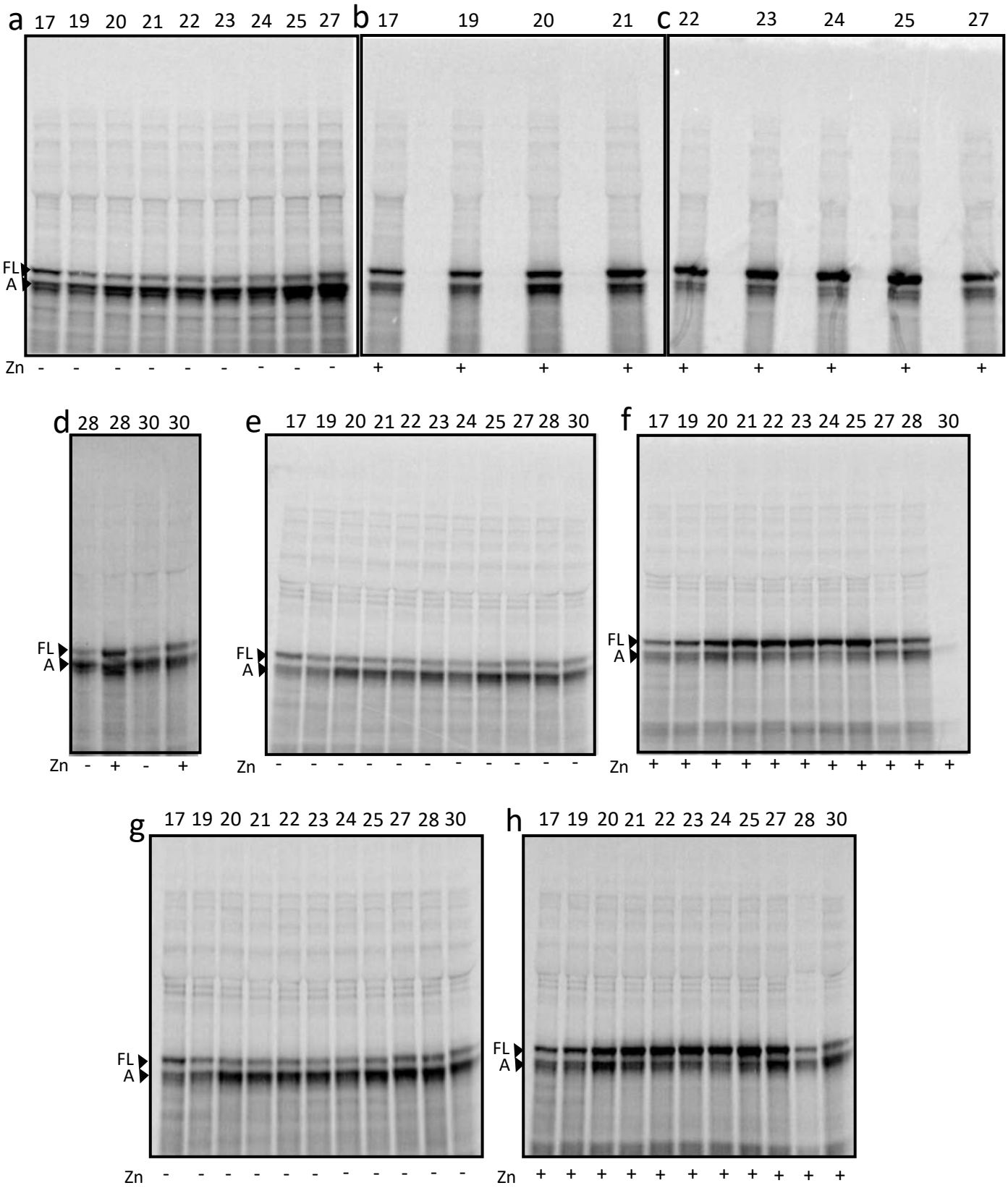

Figure 3- figure supplement 5

Translation of R16 Spectrin with WT ribosomes 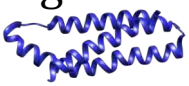

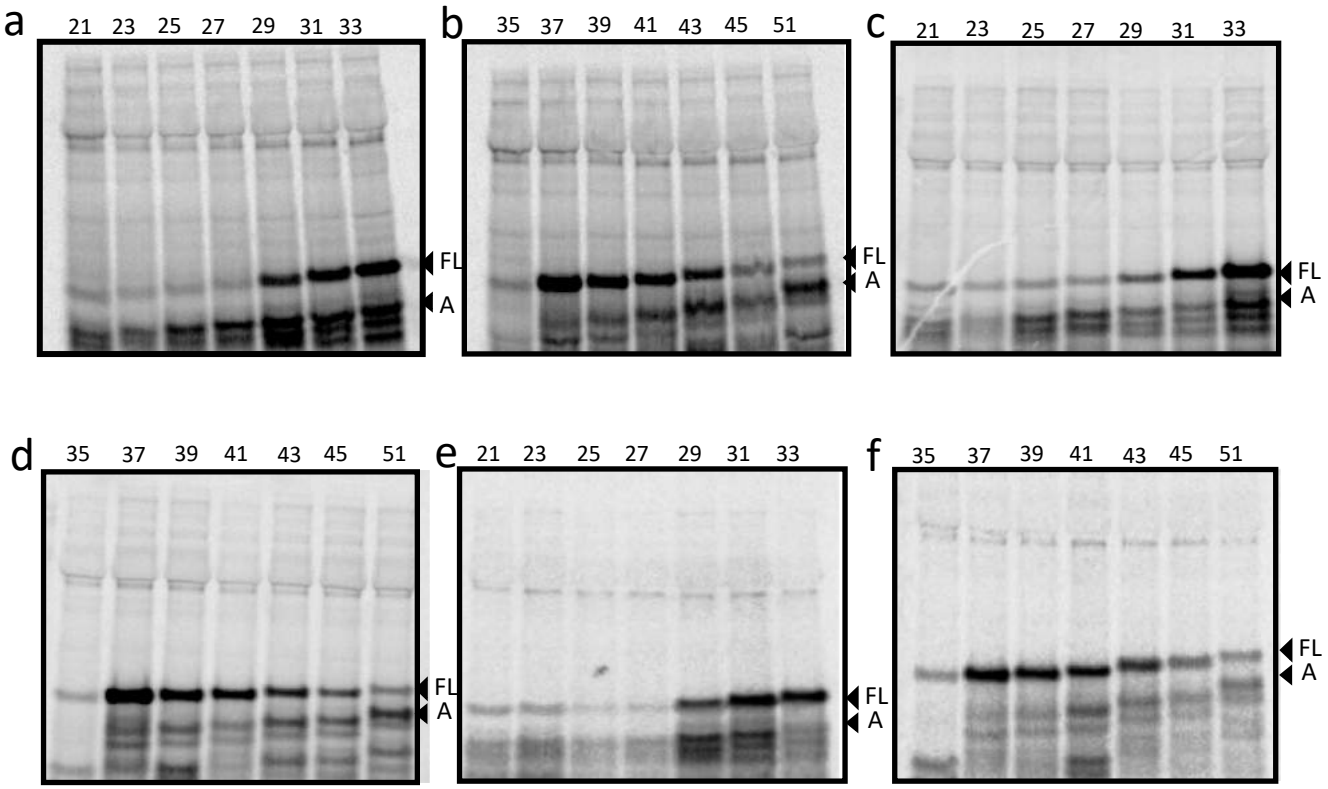

Translation of R16 Spectrin with uL23Δloop ribosomes 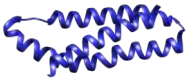

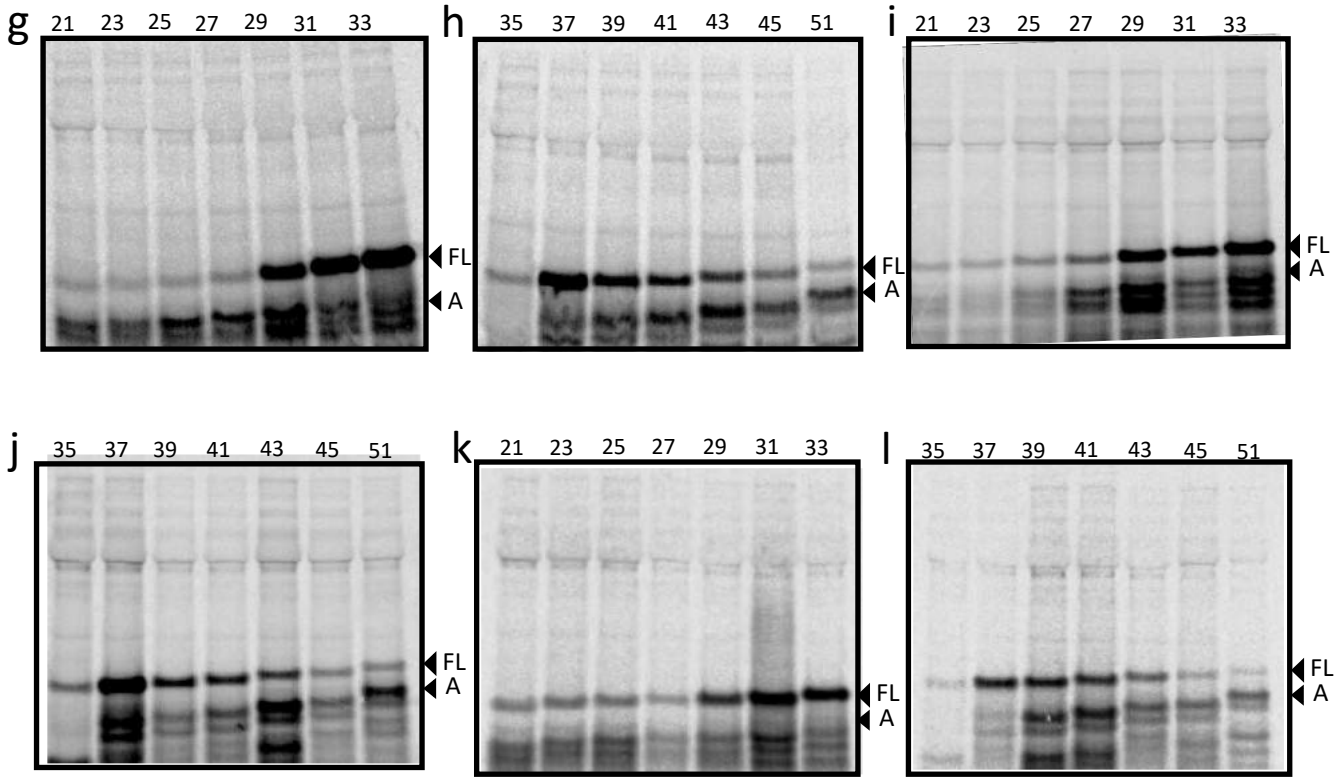

Figure 3- figure supplement 6

Translation of R16 Spectrin with uL24Δloop ribosomes

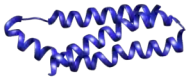

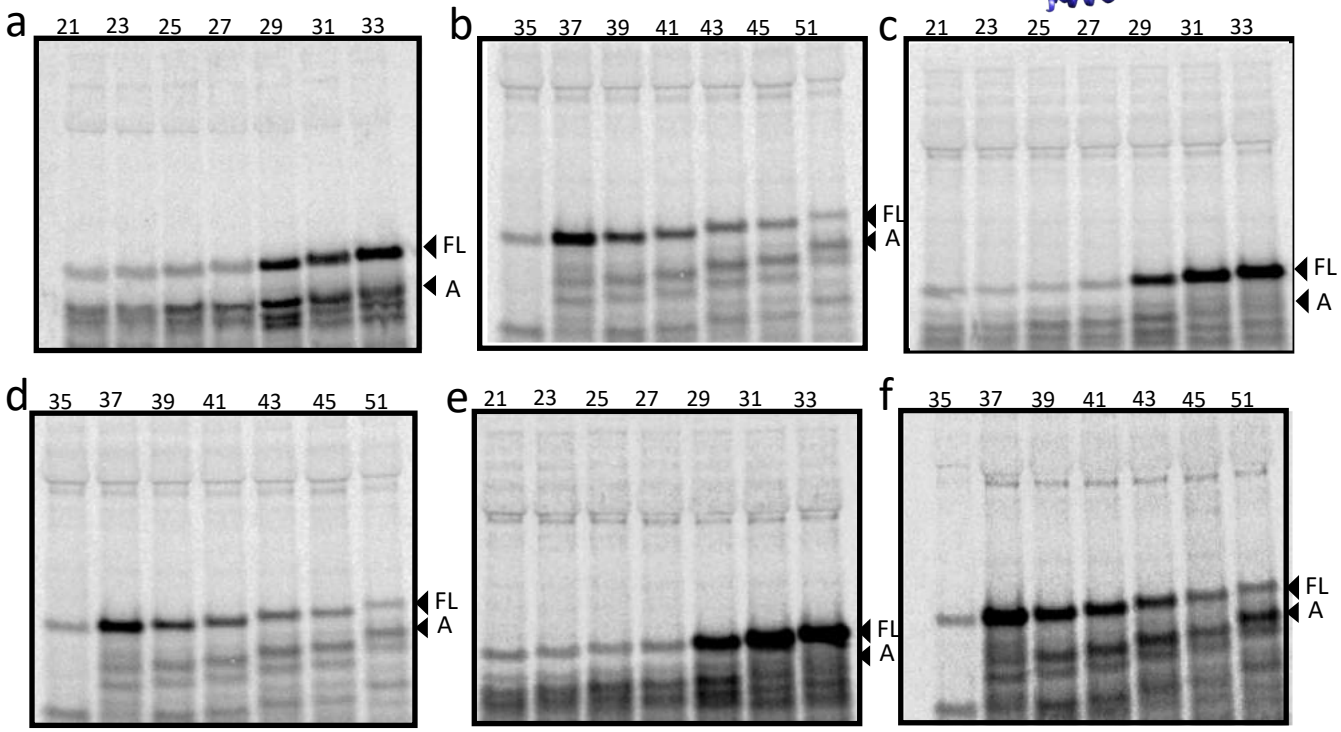

Translation of I27 Titin with WT ribosomes

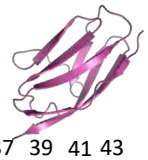

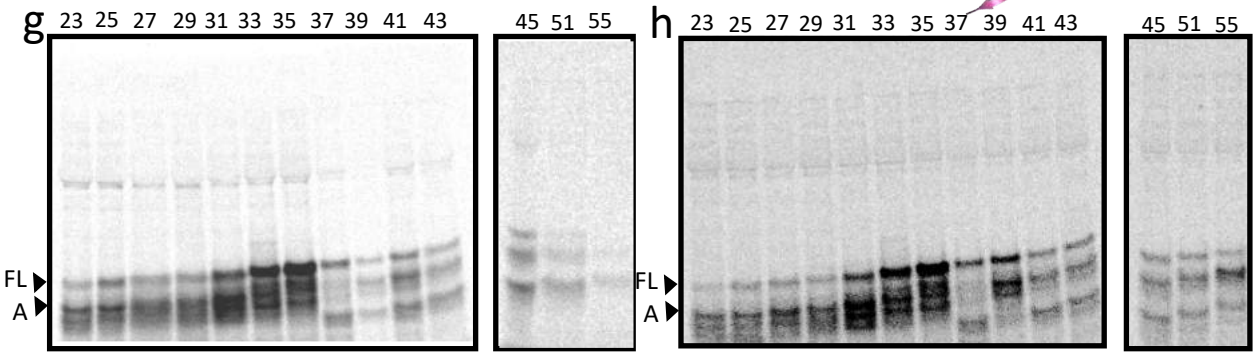

Translation of I27 Titin with uL23Δloop ribosomes

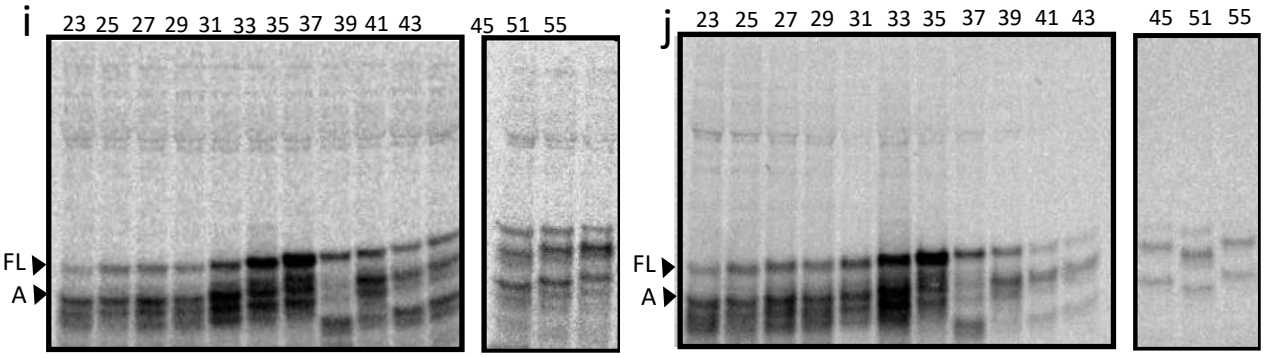

Figure 3- figure supplement 7

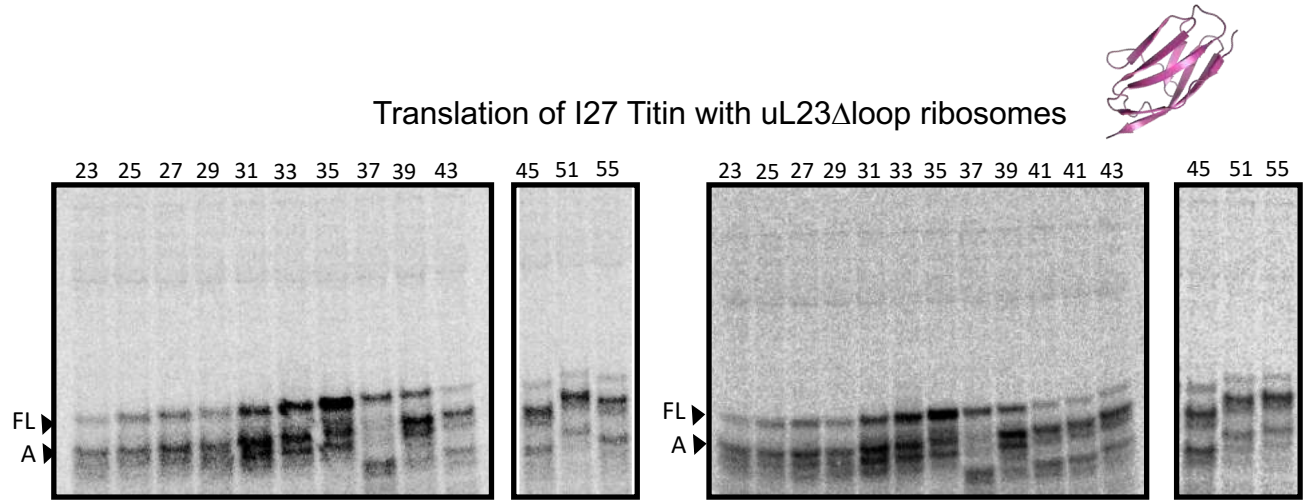

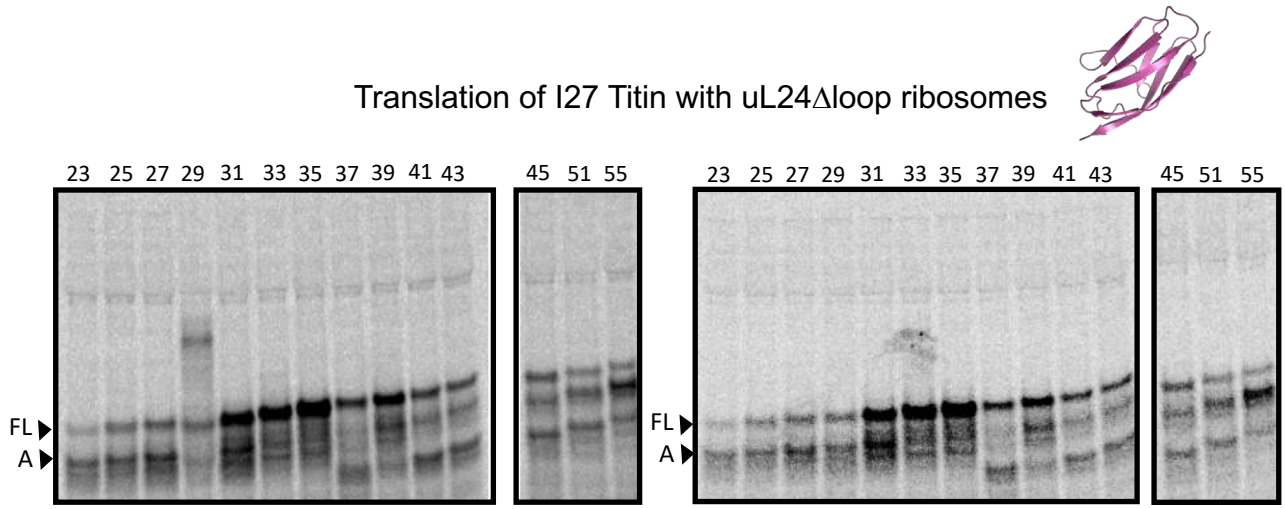

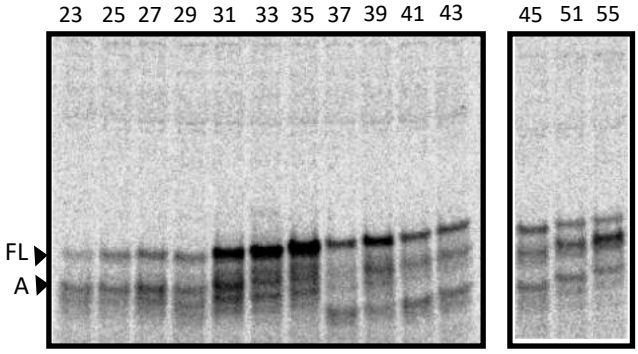

Figure 3- figure supplement 8

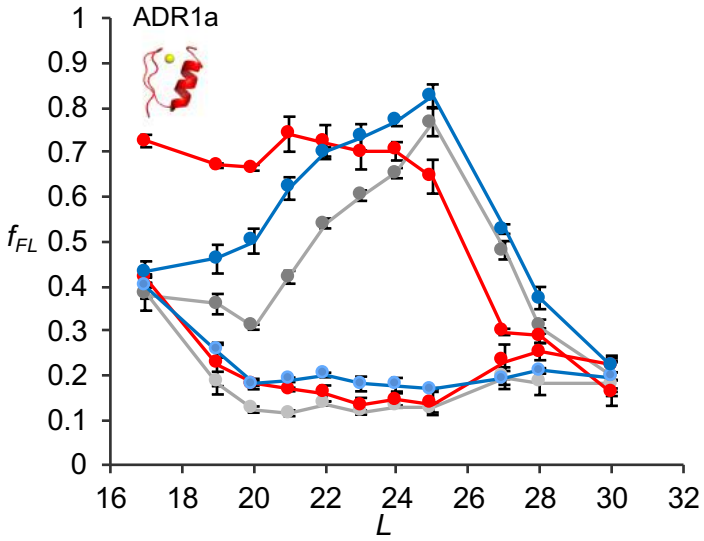

Figure 3- figure supplement 9

ADR1a

L=17

MANRSFIYEPFQIPSGSMMPTLNSTDFILVEKFAYGIKDPIYQKTLIETGHPKRGDIVVFKYPEDPK
LDYIKRAVGLPGDKVTYDPVSKELTIQPGCSSGQACENALPVTYSNVEPSDFVQTFSRRNGGEATSG
FFEVPKQETKENGIRLSETSGSGSKPYPCGLCNRCFTRRDLLIRHAQKIHSGNFSTPVWISQAQGIR
AGPGSSDKQEGEWPTGLRLSRIGGIH*

L=30

MANRSFIYEPFQIPSGSMMPTLNSTDFILVEKFAYGIKDPIYQKTLIETGHPKRGDIVVFKYPEDPK
LDYIKRAVGLPGDKVTYDPVSKELTIQPGCSSGQACENALPVTYSNVEPSDFVQTFSRRNGGEATSG
FFEVPKQETKENGIRLSETSGSGSKPYPCGLCNRCFTRRDLLIRHAQKIHSGNSGSGVPGQQWMSSF
STPVWISQAQGIRAGPGSSDKQEGEWPTGLRLSRIGGIH*

Spectrin R16

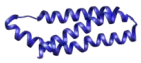

L=21

MKLNESHRLHQFFRDMDDEESWIKEKKLLVSSEDYGRDLTGVQNLRKKHKRLEAELAAHEPAIQGVL
DTGKKLSDDNTIGKEEIQQRLAQFVDHWKELKQLAAARGQRLESGSGFSTPVWISQAQGIRAGPGSS
DKQEGEWPTGLRLSRIGGIH*

L=51

MKLNESHRLHQFFRDMDDEESWIKEKKLLVSSEDYGRDLTGVQNLRKKHKRLEAELAAHEPAIQGVL
DTGKKLSDDNTIGKEEIQQRLAQFVDHWKELKQLAAARGQRLESGSGYQKTLVPGQQNATWIVPPGQ
YFMMGDWMSSFSTPVWISQAQGIRAGPGSSDKQEGEWPTGLRLSRIGGIH*

Titin I27

L=23

MRGSHHHHHHGLVPRGSGSLIEVEKPLYGVEVFVGETAHFEIELSEPDVHGQWKLKGQPLAASPDCE
IIEDGKKHILILHNCQLGMTGEVSFQAANTKSAANLKVKELSGSGFSTPVWISQAQGIRAGPGSSDK
QEGEWPTGLRLSRIGGIH**

L=53

MRGSHHHHHHGLVPRGSGSLIEVEKPLYGVEVFVGETAHFEIELSEPDVHGQWKLKGQPLAASPDCE
IIEDGKKHILILHNCQLGMTGEVSFQAANTKSAANLKVKELSGSGKFAYGIKDPIYQKTLVPGQQNA
TWIVPPGQFSTPVWISQAQGIRAGPGSSDKQEGEWPTGLRLSRIGGIH**

Figure 3- figure supplement 10

A

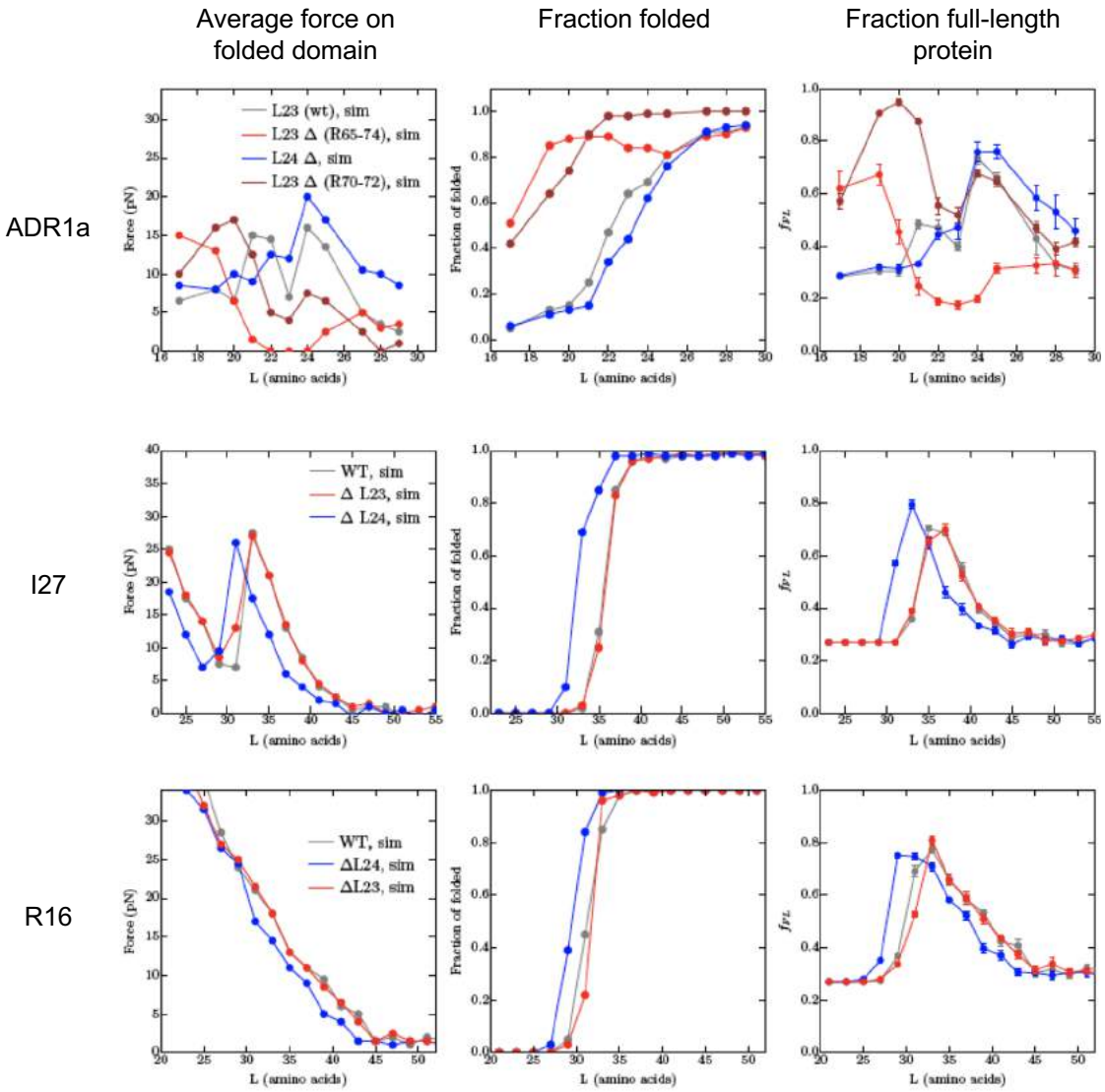

Figure 3- figure supplement 10
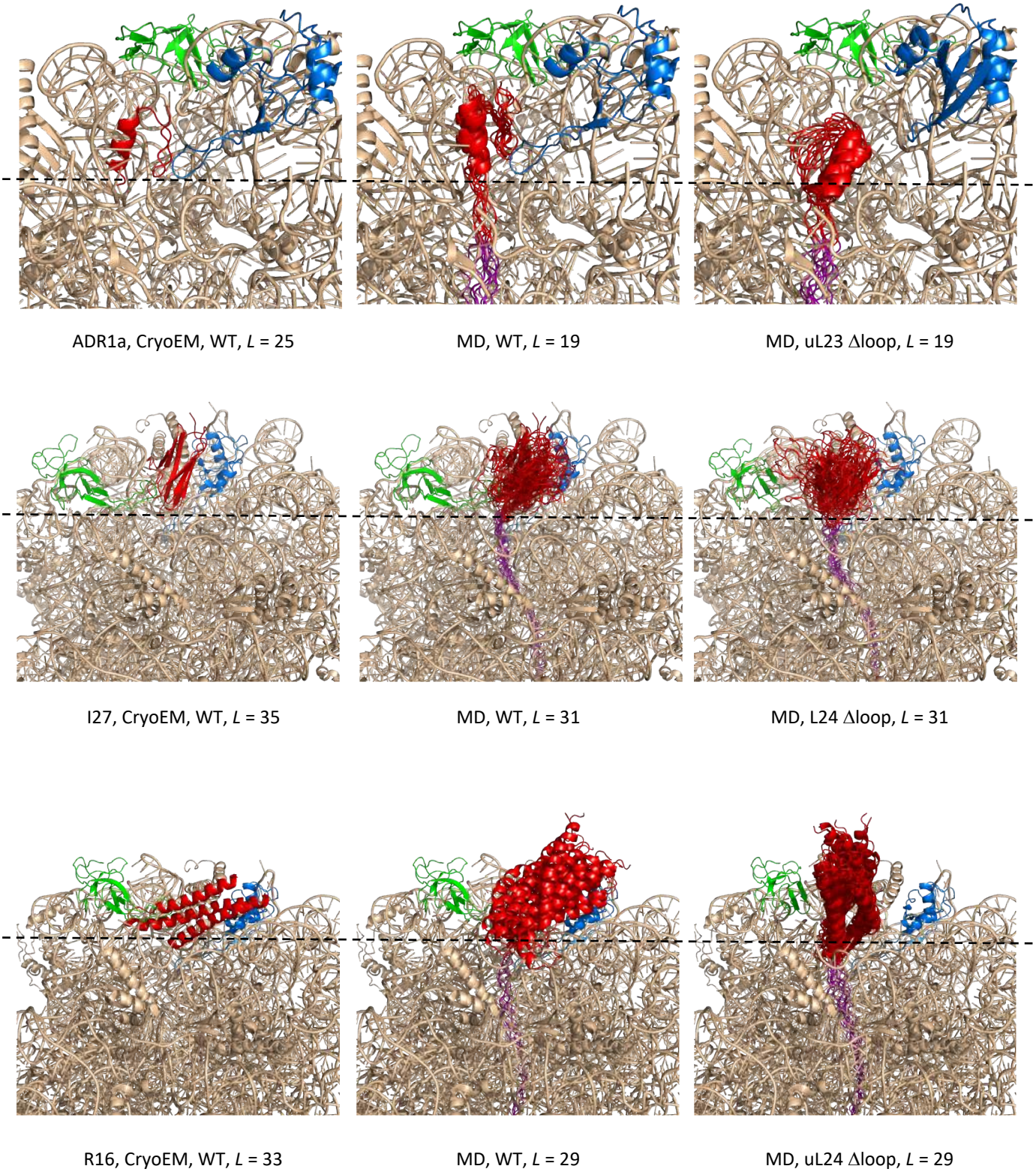
B